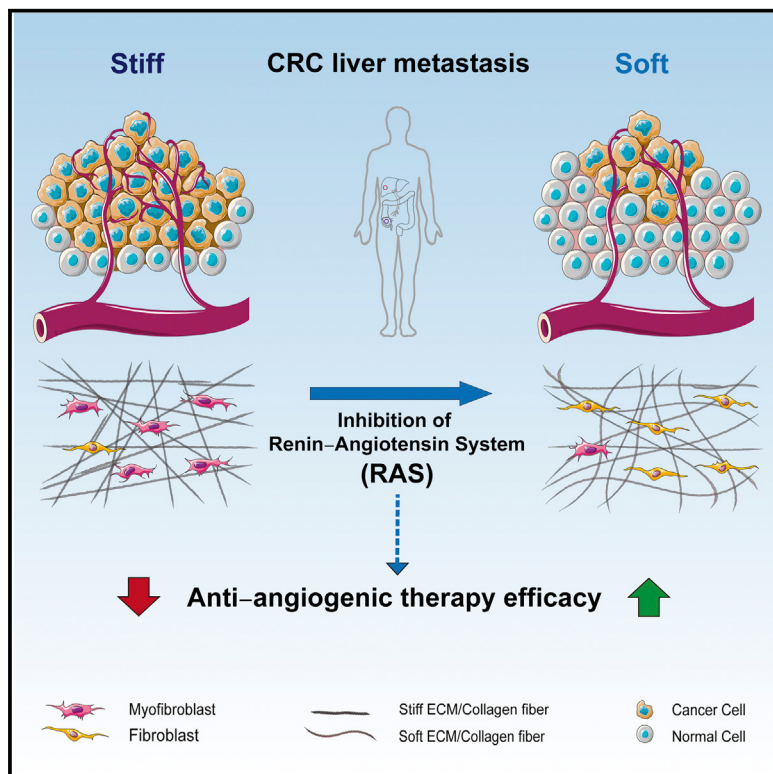


Reduction of Liver Metastasis Stiffness Improves Response to Bevacizumab in Metastatic Colorectal Cancer

Graphical Abstract



Authors

Ying Shen, Xiaohong Wang,
Junyan Lu, ...,
Carmen Ruiz de Almodovar,
Alba Díz-Muñoz, Thomas Schmidt

Correspondence

diz@embl.de (A.D.-M.),
thomas.schmidt1@
med.uni-heidelberg.de (T.S.)

In Brief

Metastatic colorectal cancer patients receiving bevacizumab have a better outcome when also receiving renin-angiotensin system (anti-RAS) inhibitors. Shen et al. demonstrate that anti-RAS inhibitors act on metastasis-associated fibroblasts to reduce tissue stiffness and increase the efficacy of anti-angiogenic therapy.

Highlights

- Highly activated metastases-associated fibroblasts (MAFs) lead to ECM stiffening
- Metastases stiffening enhances angiogenesis and anti-angiogenic therapy resistance
- Renin-angiotensin inhibition reduces MAF activity and liver metastases stiffness
- Reducing stiffness by anti-RAS drugs increases the anti-angiogenic therapy effect



Article

Reduction of Liver Metastasis Stiffness Improves Response to Bevacizumab in Metastatic Colorectal Cancer

Ying Shen,^{1,2,10} Xiaohong Wang,^{3,4,10} Junyan Lu,⁵ Martin Salfenmoser,¹ Naita Maren Wirsik,¹ Nikolai Schleussner,¹ Andrea Imle,² Aida Freire Valls,^{1,6} Praveen Radhakrishnan,¹ Jie Liang,⁷ Guoliang Wang,¹ Thomas Muley,^{8,9} Martin Schneider,¹ Carmen Ruiz de Almodovar,^{3,6} Alba Diz-Muñoz,^{2,*} and Thomas Schmidt^{1,11,*}

¹Department of General, Visceral and Transplantation Surgery, University Hospital Heidelberg, University Heidelberg, Im Neuenheimer Feld 110, 69120 Heidelberg, Germany

²Cell Biology and Biophysics Unit, European Molecular Biology Laboratory, Meyerhofstrasse 1, 69117 Heidelberg, Germany

³Biochemistry Center, University of Heidelberg, 69120 Heidelberg, Germany

⁴Department of Pharmacology and Tianjin Key Laboratory of Inflammation Biology, School of Basic Medical Sciences, Tianjin Medical University, 300070, Tianjin, China

⁵Genome Biology Unit, European Molecular Biology Laboratory, 69117 Heidelberg, Germany

⁶European Center for Angioscience (ECAS), Medical Faculty Mannheim, Heidelberg University, 68167 Mannheim, Germany

⁷Section of Molecular Immunology, Institute of Immunology, University Hospital Heidelberg, 69120 Heidelberg, Germany

⁸Thoracic Hospital, University Hospital Heidelberg, University Heidelberg, 69126 Heidelberg, Germany

⁹Translational Lung Research Centre (TLRC) Heidelberg, Member of the German Centre for Lung Research (DZL), 69120 Heidelberg, Germany

¹⁰These authors contributed equally

¹¹Lead Contact

*Correspondence: diz@embl.de (A.D.-M.), thomas.schmidt1@med.uni-heidelberg.de (T.S.)

<https://doi.org/10.1016/j.ccr.2020.05.005>

SUMMARY

Tumors are influenced by the mechanical properties of their microenvironment. Using patient samples and atomic force microscopy, we found that tissue stiffness is higher in liver metastases than in primary colorectal tumors. Highly activated metastasis-associated fibroblasts increase tissue stiffness, which enhances angiogenesis and anti-angiogenic therapy resistance. Drugs targeting the renin-angiotensin system, normally prescribed to treat hypertension, inhibit fibroblast contraction and extracellular matrix deposition, thereby reducing liver metastases stiffening and increasing the anti-angiogenic effects of bevacizumab. Patients treated with bevacizumab showed prolonged survival when concomitantly treated with renin-angiotensin inhibitors, highlighting the importance of modulating the mechanical microenvironment for therapeutic regimens.

INTRODUCTION

Colorectal cancer (CRC) is the third most common cancer worldwide (Kamangar et al., 2006) with an average 5-year overall survival (OS) of 60% (Weitz et al., 2005). Primary CRC can be cured by surgery; however, in the metastatic stage OS is substantially

reduced. In metastatic CRC (mCRC), patients undergo curative intended surgery or are treated by perioperative or palliative chemotherapy with targeted therapy (Kamangar et al., 2006; Parkin, 2001). At diagnosis 20%–30% of patients suffer from synchronous liver metastases (LM) and 50%–75% of all patients with CRC develop hepatic metastases (Jonsson et al., 2012;

Significance

Using fresh patient-derived tissues we show that widely used anti-hypertensive drugs targeting the renin-angiotensin system (anti-RAS) in combination with bevacizumab, significantly improve anti-angiogenic efficacy in metastatic colorectal cancer patients. Mechanistically, anti-RAS drugs reduce metastasis-associated fibroblast activity and thus decrease tumor stiffness. In combination with anti-angiogenic therapy, this leads to improved blood vessel integrity and longer life expectancy. This study highlights a new mechanism of action for anti-RAS drugs in cancer that could lead to new treatment modalities.



Rahbari et al., 2014), which are the leading cause of death (Taylor, 1996). To increase OS, we need to further understand mCRC and identify additional therapeutic targets. While preclinical research has focused on the primary tumor (pTU) and the metastatic process, the clinical challenge lies in the optimal treatment of metastatic patients. In addition, no commonly used immunocompetent animal model recapitulates CRC pTU and metastases growth, challenging our ability to understand CRC metastasis.

Tumor cells grow in a complex microenvironment, involving extracellular and intracellular signals that drive tumor growth, invasion, and metastasis (Hanahan and Weinberg, 2011; Northey et al., 2017). Changes in tissue mechanical properties can both precede and drive disease development (Kai et al., 2016; Northcott et al., 2018), with tumor “stiffness” correlating with prognosis in several tumor types (Colpaert et al., 2001; Laklai et al., 2016). Previous studies have shown that disease progression in several solid tumors (Mohammadi and Sahai, 2018), including breast cancer and pancreatic ductal adenocarcinoma, correlates with their elastic moduli (Laklai et al., 2016; Paszek et al., 2005).

Tissue stiffness is the extent to which a tissue resists deformation described by the relationship between stress and strain. At the tissue level, stiffness is governed by the cell’s cytoskeleton (Grady et al., 2016) and the extracellular matrix (ECM) (Humphrey et al., 2014). Fibrillar collagens are the most abundant ECM scaffolding proteins, and contribute significantly to tissue stiffness (Mouw et al., 2014). Aberrant ECM remodeling with collagen I (COL-I) enrichment has been identified as a major cause for tissue stiffening during cancer progression (Levental et al., 2009; Pickup et al., 2014). As the major source of the ECM, cancer-associated fibroblasts (CAFs) further modify the tumor mechanical environment by expressing lysyl oxidase (LOX), an amine oxidase that initiates the process of covalent intra- and intermolecular crosslinking of collagen (Kagan and Li, 2003; Levental et al., 2009). In experimental models, inhibiting matrix stiffening by LOX inhibition ameliorates tumor growth and improves therapy (Levental et al., 2009). Thus, CAFs are regarded as a promising therapeutic target for limiting cancer progression (Pickup et al., 2014).

The tumor microenvironment also plays a critical role in providing the blood supply for the tumor. mCRC angiogenesis is inhibited by targeting vascular endothelial growth factor (VEGF) signaling pathways using monoclonal antibodies, VEGF traps, or multi-targeted tyrosine kinase inhibitors (Jayson et al., 2016). Currently, insufficient efficacy and resistance limit the benefits of anti-angiogenic therapy. Moreover, endothelial cells (ECs) regulate their barrier capacity and growth according to the mechanical environment (Chien, 2007; Ingber, 2002). Specifically, a stiff matrix promotes EC proliferation and can lead to defects in vascular integrity (Huynh et al., 2011; Yeh et al., 2012), suggesting that the mechanical environment might affect EC behavior in tumors and thus affect anti-VEGF efficacy. This study aimed to elucidate if metastatic angiogenesis is affected by the mechanical microenvironment, which can be modulated by metastasis-associated fibroblast (MAF) activation in mCRC, and if this MAF activation can be altered to increase the efficacy of anti-angiogenic therapy.

RESULTS

MAFs in CRC Are Highly Activated

To investigate the fibroblast signature between pTUs and LM in CRC patients, we performed stainings for the fibroblast marker platelet-derived growth factor receptor (PDGFR α), the myofibroblasts markers α -smooth muscle actin (α SMA), phospho-myosin light chains 2 (p-MLC2) (actomyosin contractility), and for the ECM component COL-I (Figures 1A–1C). A significant higher expression of α SMA, p-MLC2, and COL-I was observed in LM, suggesting myofibroblast and ECM remodeling features of MAFs (Figures 1D–1F).

Next, primary fibroblasts were isolated from pTUs (CAFs) and LM (MAFs) of CRC patients. MAFs showed a significant upregulation of α SMA and p-MLC2 (Figures 1G–1K and S1A), validating an increased myofibroblast and cellular contractility signature. Consistently, MAFs showed a significant upregulation of ACTA2 (α SMA), COL1A1 (collagen type I alpha 1), and LOX (lysyl oxidase) mRNA (Figures S1B–S1D). Such MAFs are liver derived, as expression of the fibroblast-specific protein 1 (encoded by S100A4), which identifies an inflammatory subpopulation of macrophages (and not fibroblasts) in the liver, was significantly reduced (Osterreicher et al., 2011) (Figure S1E).

Focal adhesions (FAs) (Northcott et al., 2018) facilitate cell adhesion, migration, cytoskeleton regulation, and matrix remodeling (Kuo et al., 2011; Oakes et al., 2012). FAs depend on tensile forces generated within and outside the cell (Dugina et al., 2001; Hinz et al., 2003). An elongation or super-maturation of FAs is seen during fibroblast-to-myofibroblast transition (Dugina et al., 2001). Quantification of FAs showed a larger average area of FAs in MAFs (Figures 1L and 1M) with an increase of super-mature FAs (Figures S1F and S1G), supporting that CRC MAFs are highly activated.

ECM Remodeling and Stiffening Features in Advanced CRC Patients

To identify gene expression signatures associated with liver metastasis we performed RNA sequencing (RNA-seq) on pTUs and LM of CRC patients (Figure 2A; Table S1). Gene set analysis (GSA) of upregulated genes in LM using the Pathway Interaction Database (PID) revealed a significant enrichment in integrin signaling (Schaefer et al., 2009) (Figure 2B). Integrins are ECM receptors and function as mechanotransducers. Increased integrins in tumors promote malignancy by transducing ECM queues to cytoskeletal structures (Paszek et al., 2005). This supports a role for fibroblasts as tumor ECM remodeling is largely dependent on them (Lampi and Reinhart-King, 2018).

To further characterize the gene expression of fibroblasts, we performed RNA-seq on isolated primary CAFs and MAFs (Figure 2C; Table S1b) after successful enrichment (Figure 2D). We identified 3,721 differentially expressed genes (Figure 2E). Gene ontology (GO), Kyoto Encyclopedia of Genes and Genomes (KEGG), and PID were used to predict the functional role of the differently expressed genes (Figures 2F–2H). GO identified upregulated myofibroblasts/ECM remodeling features in MAFs (Figure 2F; Table S2). KEGG identified ECM-receptor interactions and FA features (Figure 2G) and PID integrin signaling (Figure 2H), with a significant upregulation of ITGAV, ITGB1, and FN1 (fibronectin) in MAFs (Figure S2A), which are critical for

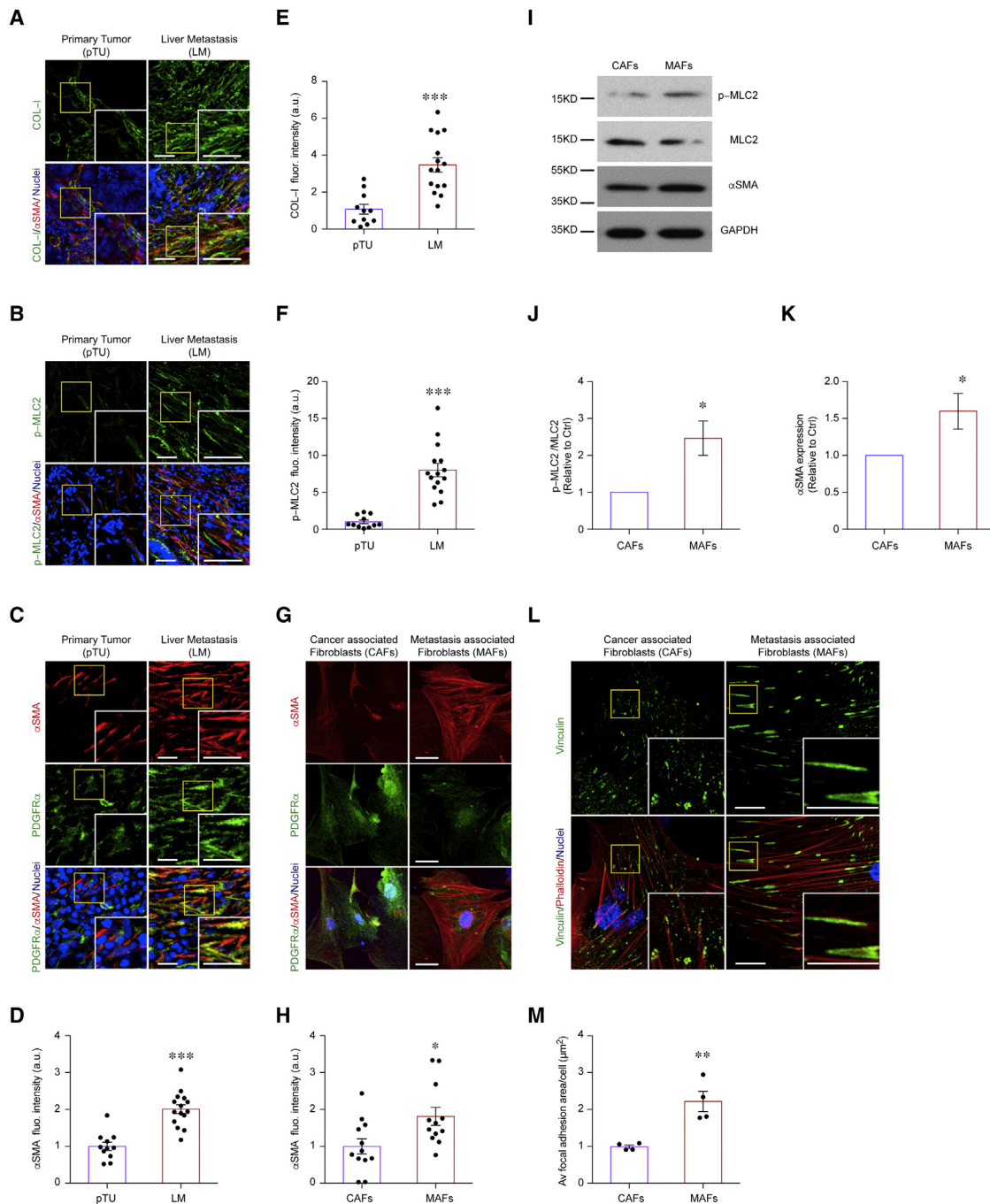


Figure 1. Different Stroma Activation in Primary Tumors and Liver Metastases

(A–C) Immunostainings of (A) COL-I (green) and αSMA (red), (B) p-MLC2 (green) and αSMA (red), and (C) PDGFRα [green]) and αSMA (red) on pTU und LM paraffin sections.

(D–F) Quantification of (D) αSMA fluorescence intensity ($p < 0.0001$; $t = 5.874$, $df = 24$), (E) p-MLC2 fluorescence intensity ($p < 0.0001$; $t = 6.511$, $df = 24$), and (F) COL-I fluorescence intensity ($p < 0.0001$; $t = 4.677$, $df = 24$) (all $n = 11$ pTU/15 LM).

(G) Immunostainings of αSMA (red) and PDGFRα (green) in cultured CAFs/MAFs from pTU and LM.

(H) Quantification of αSMA fluorescence intensity ($n = 12/12$; $p = 0.018$; $t = 2.567$, $df = 22$) in cultured CAFs/MAFs.

(I–K) Western blot (I) and quantification of (J) p-MLC2/MLC2 ($n = 3/3$; $p = 0.035$; $t = 3.148$, $df = 4$) and (K) αSMA ($n = 5/5$; $p = 0.038$; $t = 2.485$, $df = 8$) in cultured CAFs/MAFs.

(L) Immunostainings of the FA marker Vinculin (green) and F-actin (phalloidin [red]) in cultured CAFs/MAFs.

(M) Quantification of average FAs area of individual cells ($n = 4/4$; $p = 0.005$; $t = 4.398$, $df = 6$).

In all panels: * $p < 0.05$, ** $p < 0.01$, *** $p < 0.001$. Values as mean \pm SEM and compared by unpaired Student's t test. Scale bars, 20 μm in (A–C) and (L) and 35 μm in (G). au, arbitrary unit. See also Figure S1.

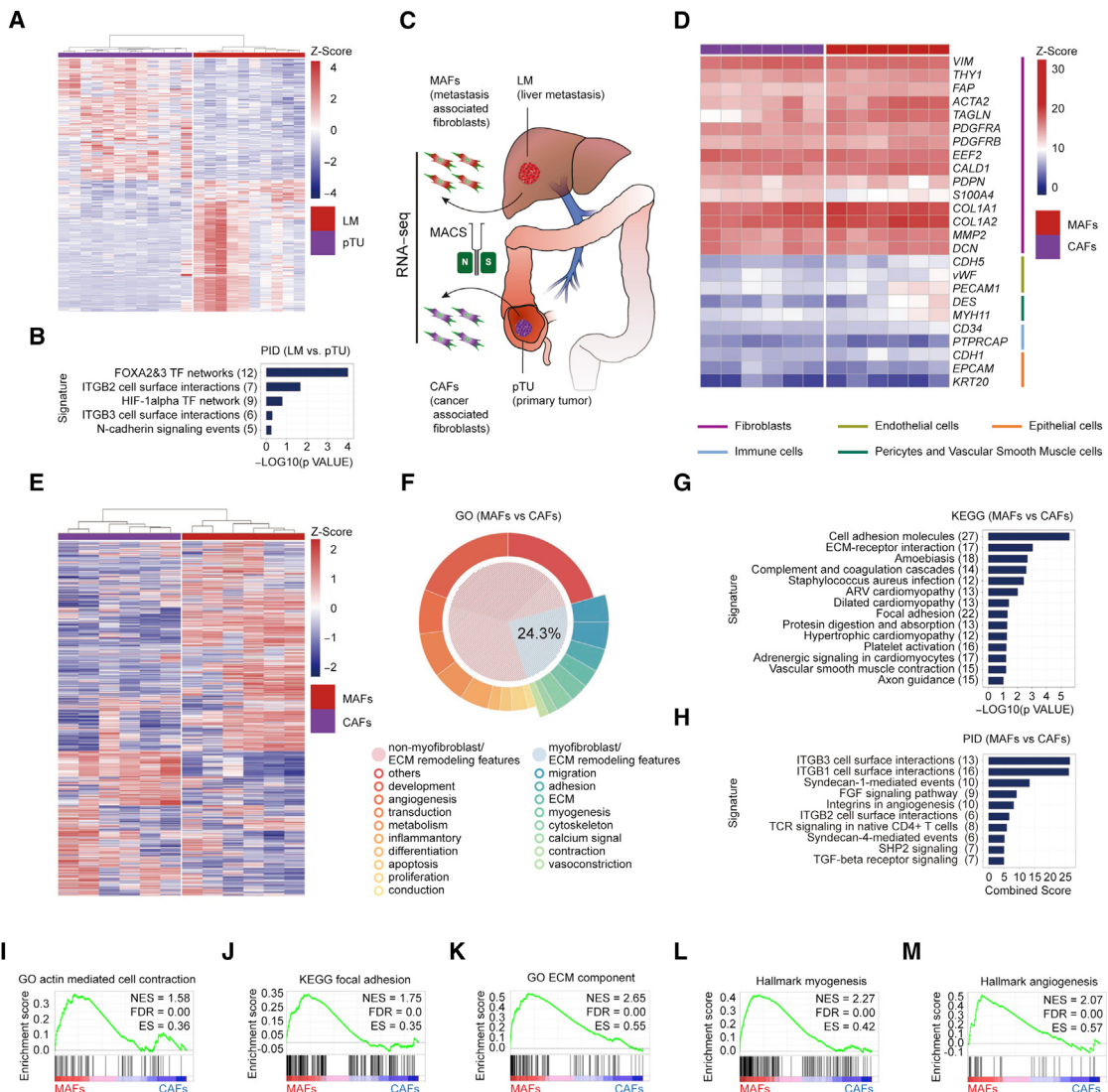


Figure 2. MAFs Are Highly Activated in Comparison to CAFs

(A) Heatmap of 2,226 differentially expressed genes in pTU (purple) and LM (red) (1,232 downregulated and 994 upregulated in LM versus pTU ($n = 12$ and 10; all absolute \log_2 fold change >0.5 , false discovery rate [FDR] $<10\%$).

(B) PID (Pathway Interaction Database) annotation of enrichment pathways of top 1,000 significantly (FDR $<5\%$) upregulated genes in LM versus pTU.

(C) Scheme of cell isolation for RNA-seq (magnetic-activated cell sorting [MACS]).

(D) Heatmap of fibroblast marker genes in isolated CAFs/MAFs ($n = 6$ CAFs/6 MAFs).

(E) Heatmap of 3,721 differentially expressed genes in isolated CAFs (purple) and MAFs (blue) (1,981 downregulated and 1,740 upregulated in MAFs) ($n = 6/6$; all absolute \log_2 fold change >0.5 , FDR $<5\%$).

(F–H) GSA of top 1,000 significantly (FDR $<5\%$) upregulated genes of MAFs versus CAFs with (F) GO annotation, (G) KEGG annotation, and (H) PID annotation of enrichment pathway features.

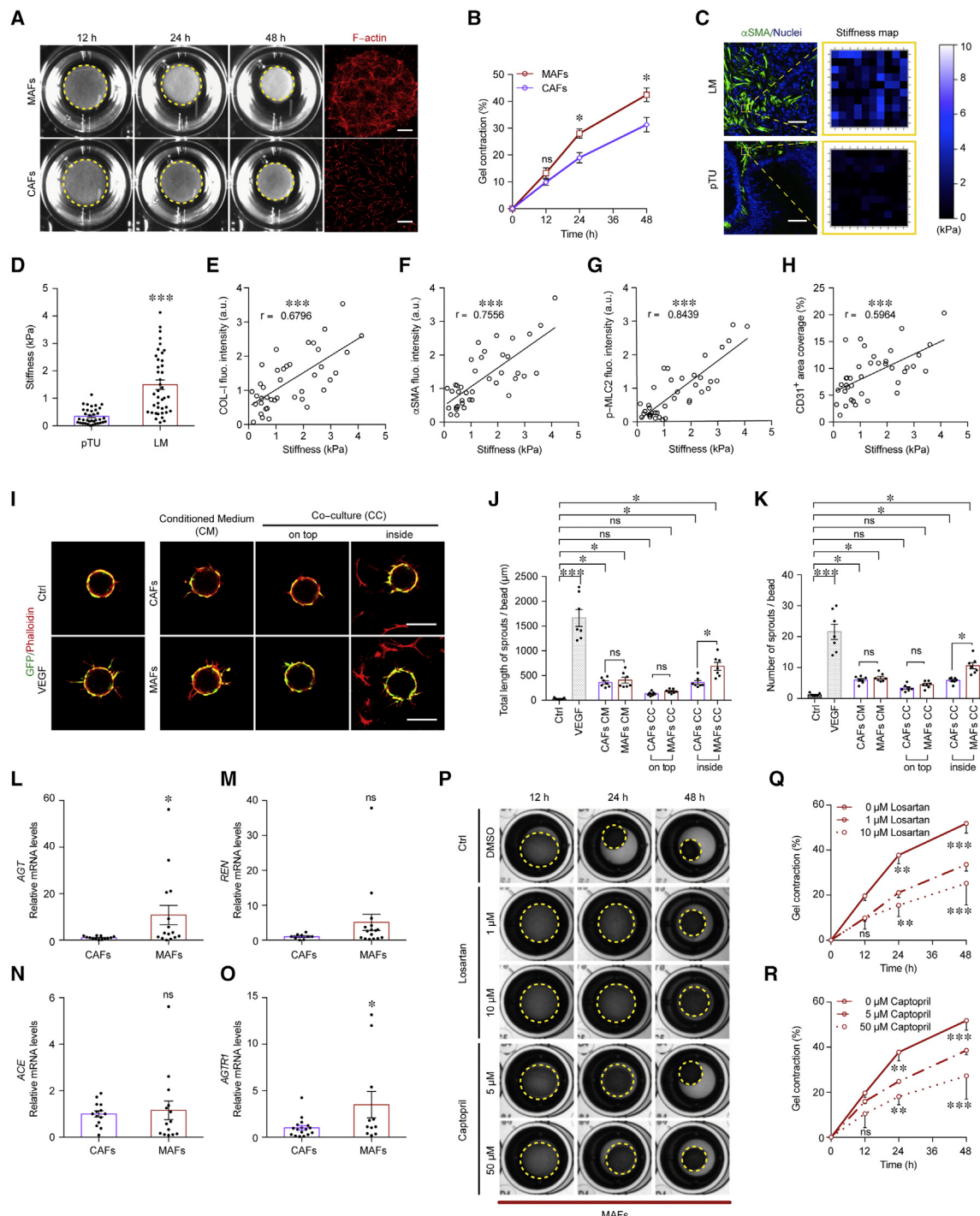
(I–M) GSEA of the top 1,000 upregulated genes showing (I) GO (actin-mediated cell contraction), (J) KEGG (focal adhesion), (K) GO (extracellular matrix component), (L) Hallmark (myogenesis), and (M) Hallmark (angiogenesis). ES, enrichment score; NES, normalized enrichment score.

In (B), (G), and (H), the number of genes upregulated inside the indicated pathway are in parentheses. See also Figure S2 and Tables S1 and S2.

tissue fibrosis (Reed et al., 2015). In addition, gene set enrichment analysis (GSEA) (Subramanian et al., 2005) also revealed a strong enrichment of actin-mediated cell contraction, FA, ECM components, myogenesis, and angiogenesis signatures for differentially expressed genes (Figures 2I–2M).

To corroborate the relevance we performed a consensus clustering analysis (Guinney et al., 2015) on RNA-seq data from 451 patients with primary CRC, which identified 7 transcriptomic

clusters (TCGA-COAD) (Cancer Genome Atlas, 2012) (Figures S2B and S2C). By pathway analysis to understand the biological signatures of the groups (Guinney et al., 2015; Yoshihara et al., 2013), we observed that cluster 1 showed a mesenchymal signature with active stroma and angiogenesis features (Figure S2D; Table S2), matching our results from isolated MAFs. Patients in cluster 1 showed a significant reduction in survival in comparison with patients in cluster 7, the one with the best OS (Figure S2E).

**Figure 3. MAFs Promote Angiogenesis by Increasing ECM Stiffness**

(A) Gel contraction assay of CAFs and MAFs. Left: representative images of gel contraction over time. Contracted gel within yellow line. Right: F-actin staining (Phalloidin) of CAFs/MAFs after 72 h of culture in the gels.

(B) Quantification of gel contraction over time (n = 9 CAFs/8 MAFs; p = 0.553/0.003/0.0002).

(C) Left: immunostainings of α SMA (green). Right: stiffness maps of yellow outlined area from cryosections of pTU and LM.

(D) Quantification of average tissue stiffness in pTU (n = 36) and LM (n = 40) as in (C) (p < 0.0001; t = 6.111, df = 74).

(E–G) Pearson correlation comparison analysis of tissue stiffness and fluorescent intensity of COL-I (E), α SMA (F), and p-MLC2 (G) in LM in patient samples. (n = 40; all p < 0.0001).

(H) Pearson correlation comparison analysis of tissue stiffness and vessel density indicated by percent of CD31⁺ area staining (n = 40; p < 0.0001).

(legend continued on next page)

To understand the impact of stroma-related gene expression, we performed GSA on the top differentially regulated genes in cluster 1 versus 7 to identify altered biological processes using GO (Table S2), KEGG, and PID. A large fraction (33.8%) of GO terms were linked to myofibroblasts/ECM remodeling features (Figure S2F). Further ECM-receptor signaling, FAs, and integrin signaling are cluster 1 features (Figures S2G and S2H). GSEA revealed actin-mediated cell contraction, ECM components, myogenesis, ECM assembly, and FAs as highly enriched signatures in cluster 1 (Figures S2I–S2M). Notably, sprouting angiogenesis was also identified as a cluster 1 feature (Figure S2N). While VEGF showed no difference in expression, VEGFR2 (KDR) is highly expressed in cluster 1 (Figure S2O).

The above results suggest that activated fibroblasts might correlate with an advanced disease and worse prognosis, as observed in other tumors (Colpaert et al., 2001, 2003; Hu et al., 2018). Next, we aimed to elucidate whether the observed gene signature also translates to a strong contractility and matrix remodeling ability of MAFs.

MAFs Increase Microenvironment Stiffness, which Supports Angiogenesis

Fibroblasts facilitate matrix remodeling through active contraction, leading to matrix stiffening (Calvo et al., 2013). We performed gel-remodeling assays and observed that MAFs displayed a denser and more complex F-actin network (Figure 3A) and could contract gels to a greater extent than CAFs (Figure 3B). This effect was not due to changes in cell proliferation, suggesting a high matrix remodeling ability of MAFs (Figure S3A).

To assess if higher MAF activation leads to mechanical changes in the microenvironment in CRC patients, we quantified tissue stiffness in pTUs and LM using atomic force microscopy (AFM) (Figures S3B–S3M). In fresh and cryo-preserved tissues we observed a significant increase in stromal stiffness in LM (Figures 3C, 3D, S3J, and S3K). Stiffness correlated with COL-I, α SMA, and p-MLC2 expression in samples from the same patients (Figures 3E–3G). Unlike LM, CRC lung metastases are not stiffer than pTUs (Figure S3N) and show lower stroma activation (Figure S3O). In line it has been shown that CRC lung metastases have fewer MAFs than LM (Tommlein et al., 2015).

Matrix stiffening regulates EC proliferation, angiogenesis, vessel outgrowth, and branching (Bordeleau et al., 2017; Mammo et al., 2009; Yeh et al., 2012). To investigate this link, we assessed the vasculature in LM and observed a correlation between stiffness and CD31 $^{+}$ vascular area (Figure 3H). To further evaluate the influence of fibroblasts on angiogenesis, we performed sprouting angiogenesis assays. Fibroblasts promote

angiogenesis by secreting cytokines, as the use of conditioned medium (CM) from CAFs and MAFs leads to an increased EC sprouting (Figures 3I–3K). However, CM failed to reveal a difference between CAFs and MAFs. Culturing of fibroblast cells on top of the collagen gel did not show a difference either. Interestingly, when cultured within the gel, which allows fibroblast to remodel the matrix, MAFs induced EC sprouting to a significantly greater extent than CAFs (Figures 3I–3K). Thus, MAFs support sprouting angiogenesis by cytokines with concomitant local ECM remodeling.

Renin-Angiotensin System Inhibition Target Fibroblasts

To test if metastasis stiffening could affect angiogenesis and thus CRC prognosis, we aimed at targeting MAF hyper-activation to reduce stiffening. To identify disease signatures (excluding the tumor signature) in our bioinformatics comparisons (LM versus pTU, MAFs versus CAFs, and TCGA cluster 1 versus 7), we used a Jensen diseases database under the interactive gene list enrichment analysis platform “Enrichr” (Chen et al., 2013). We observed a hypertension disease signature in LM, MAFs, and in cluster1 (Figures S4A–S4C). Moreover, using GSEA on KEGG gene sets we observed that the vascular smooth muscle contraction signaling pathway was significantly enriched in MAFs and in cluster 1 (Figures 2G, S2G, S4D, and S4E).

Vascular smooth muscle contraction, together with arterial remodeling, are hallmarks of hypertension, a disease regulated among others by the renin-angiotensin system (RAS), the sympathetic nervous system, immune activation and oxidative stress (Lacolley et al., 2017; Vaziri and Rodriguez-Iturbe, 2006). Liver fibroblasts express the RAS system component angiotensin II (ANGII) (Bataller et al., 2003), and ANGII stimulation triggers liver fibrosis by activating the ANGII type I receptor (AT1R or AT-1) (Granzow et al., 2014). qPCR analyses on freshly isolated MAFs versus liver-derived fibroblasts revealed a significant increase in expression of all the key components of the RAS system (angiotensinogen [AGT], renin [REN], angiotensin converting enzyme [ACE], and AT-1 [AGTR1]) (Figures S4F–S4I). In addition, MAFs expressed significantly higher levels of AGT and AGTR1 than CAFs (Figures 3L–3O).

To characterize the impact of RAS targeting on MAF function, we performed gel contraction assays upon treatment with losartan (an AT-1 blocker) or captopril (an ACE inhibitor). Both significantly reduced MAF gel contraction at low (1 μ M for losartan and 5 μ M for captopril) and at high (10 μ M for losartan and 50 μ M for captopril) concentrations (Figures 3P–3R). This effect is not due to changes in cell proliferation (Figures S4J and S4K). Treatment with losartan or captopril failed to reduce the gel contraction of

(I) EC sprouting assay of GFP+ HUVECs with CAF/MAF-derived conditioned medium (CM) or co-cultured (CC) with the same number of fibroblasts on top or inside the gel. Immunostaining of F-actin (phalloidin [red]) of all cell populations. VEGF (50 ng/mL) as positive control.

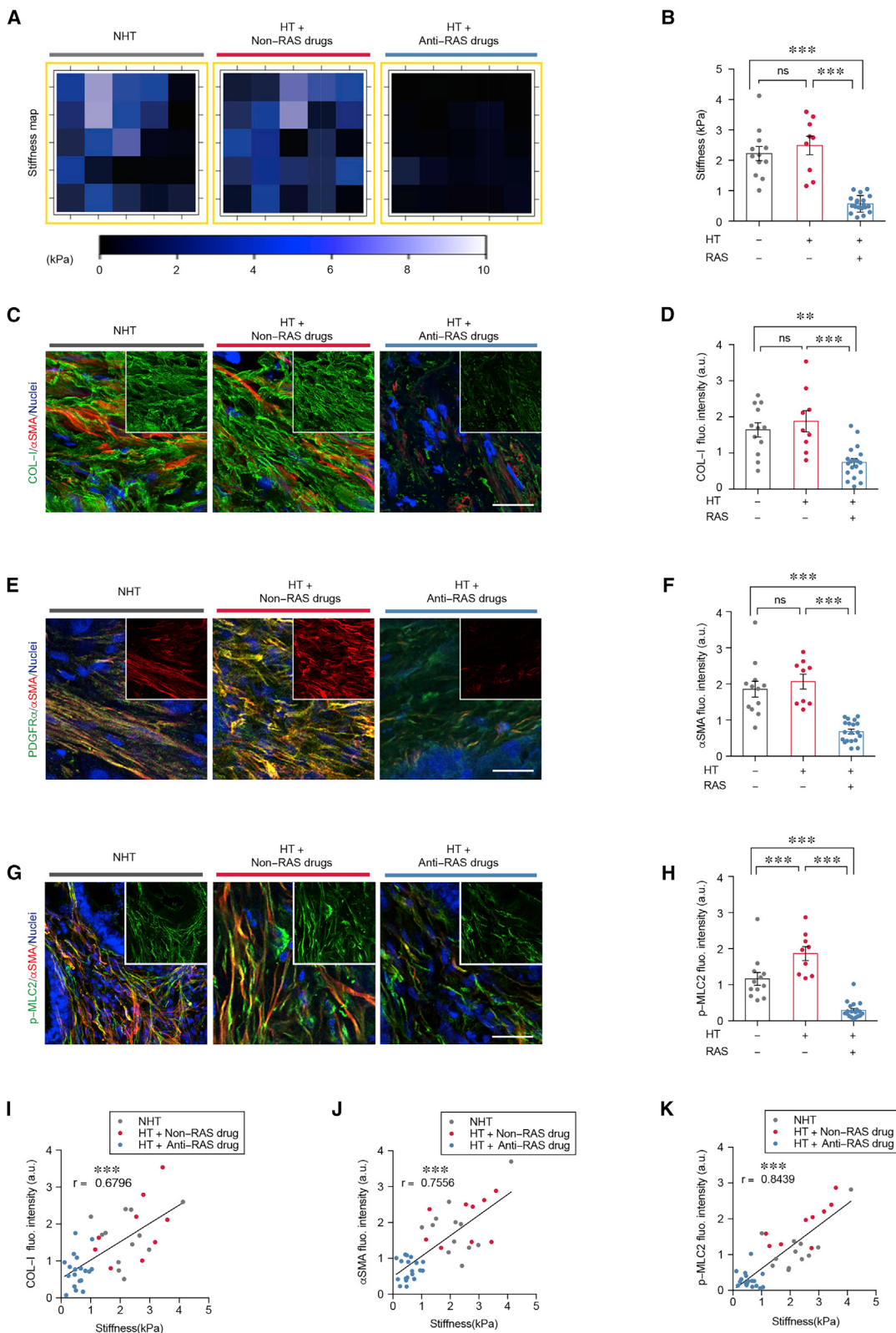
(J and K) Quantification of total sprout length in (J) ($F = 52.02$, $df = 55$) and number of sprouts in (K) ($F = 40.08$, $df = 55$) per bead ($n = 7$ biological repeats, 20 beads/dot [one biological repeat]).

(L–O) qPCR analysis of (L) AGT ($p = 0.038$; $t = 2.182$, $df = 26$), (M) REN ($p = 0.208$; $t = 1,295$, $df = 23$), (N) ACE ($p = 0.719$; $t = 0.3634$, $df = 26$), and (O) AGTR1 ($p = 0.043$; $t = 2.217$, $df = 26$) mRNA in CAFs/MAFs ($n = 9$ –14 CAFs/11–16 MAFs).

(P) Gel contraction assay of MAFs with losartan or captopril treatment at different time points. Contracted gel within yellow line.

(Q and R) Quantification of gel contraction under losartan ($F = 10.35$, $df = 45$) (Q) and captopril ($F = 8.03$, $df = 45$) (R) treatment over time as shown in (P) ($n = 6$ each conditions).

In all panels: * $p < 0.05$, ** $p < 0.01$, *** $p < 0.001$. Scale bars, 200 μ m (A and I) and 50 μ m (C). Stiffness maps, 20 \times 20 μ m (C); values as mean \pm SEM and compared by unpaired Student’s t test in (D) and (L–O); one-way ANOVA multiple comparisons with Tukey’s method among groups in (J) and (K) and two-way ANOVA with Sidak’s method among groups in (B), (Q), and (R). See also Figures S3 and S4.

**Figure 4. RAS Inhibitors Reduce ECM Stiffness**

(A and B) Stiffness map (A) and stiffness quantification (B) of LM stroma area from mCRC patients: n = 12 (no hypertension [NHT] patients), 9 (hypertension [HT] + non-RAS drugs), and 19 (HT + RAS drugs); F = 38.33, df = 37.

(legend continued on next page)

CAFs (Figures S4L–S4N). However, ANGII treatment can strongly induce CAF contraction to a similar extent as MAFs. Under this condition losartan can block the increased contractility, suggesting that the initially low inhibitory effect on CAFs is a result of the low expression of RAS components (Figures S4O–S4R). Inhibition and stimulation of the AT-2 receptor did not affect MAF and CAF gel contraction (Figures S4S and S4T).

RAS Inhibition Reduces Metastasis Stiffness and Remodels the Microenvironment

Based on these *in vitro* findings, we evaluated if RAS inhibition in patients leads to similar effects on metastasis stiffness by quantifying tissue stromal stiffness by AFM in LM tissue samples. Patients were divided into three groups: (1) no hypertension; (2) hypertension treated with non-RAS drugs; and (3) hypertension treated with anti-RAS drugs (Table S3). Patients treated with anti-RAS drugs showed a significant reduction in tissue stiffness when compared with the no hypertension group and the non-RAS-treated group 2 (Figures 4A and 4B). Thus, the level of activation of the RAS system, but not the presence of hypertension, is a major determinant of tissue stiffness in patients.

We further assessed (by staining for COL-I, α SMA, and p-MLC2 in the same patient groups) if differences in metastasis stiffness could be explained by a downregulation of MAF activation. While hypertension correlated with an increase in p-MLC2 staining, we did not observe an effect on α SMA and COL-I (Figures 4C–4H). Across all groups, anti-RAS treatment showed a significant reduction of MAF activation and ECM deposition (Figures 4C–4H). The effects of anti-RAS drugs were independent of the specific RAS inhibition treatment (Figures S5A–S5C). A positive correlation between metastases stiffness (with different conditions \pm hypertension \pm anti-RAS drugs) and COL-I, α SMA, and p-MLC2 expression was observed (Figures 4I–4K), suggesting that the level of MAF activation contributes to tissue stiffness in LM. In summary, patients with anti-RAS treatment show a low myofibroblasts/ECM signature that explains the decrease in metastases stiffening.

Anti-RAS treatment also further reduces the lower stiffness of pTUs (Figure S5D and S5E; Table S3). Moreover, similarly to LM, pTU stiffness correlated with COL-I and α SMA levels (Figures S5F–S5J). Anti-RAS treatment led to a reduction of COL-I and α SMA (Figure S5H and S5K), while hypertension without anti-RAS treatment did not (Figures S5H and S5K). However, p-MLC2 expression was not changed and did not correlate with pTU stiffness (Figures S5L–S5N).

AT1R Signaling Mediates MAF Activation via RhoA

Next, we wanted to determine how RAS inhibition leads to a reduction in MAF activation. Treatment of MAFs with losartan or captopril *in vitro* demonstrated a decrease of LOX and COL1A1 mRNA expression (Figures 5A and 5B). p-MLC2 is also significantly reduced upon RAS inhibition (Figures 5C and 5D). During the pathogenesis of hypertension, RhoA mediates ANGII-induced contraction by triggering the phosphorylation of myosin phosphatase (Bai et al., 2013; Guilluy et al., 2010). The Rho guanine nucleotide exchange factor ARHGEF1 mediates contraction in vascular smooth muscle cells, and Tyr738 phosphorylation is mediating activation of ARHGEF1 for this effect (Guilluy et al., 2010). Losartan and captopril treatment significantly reduced tyrosine phosphorylation of ARHGEF1, and led to a reduction of active RhoA (Figures 5E–5H). Similarly, knockdown of the ARHGEF1 leads to a reduction of p-MLC2, supporting a role for the angiotensin-ARHGEF1-RhoA axis in MAFs (Figures 5I, 5J, and S6A). Collectively, we propose that RAS pathway inhibitors block matrix stiffening via inhibition of MAF active contraction (Figure 5K) as well as a reduction of collagen production and crosslinking, thus ameliorating the tumor fibrosis process.

RAS Inhibition Increases the Anti-angiogenic Effect of Bevacizumab

Given that high tissue stiffness correlated with vascular density in patients (Figure 3H) and that metastases stiffness was reduced in patients treated with RAS-inhibiting drugs (Figures 4A and 4B), we assessed if altered stiffness could affect the efficacy of anti-angiogenic treatment. As model systems for mCRC have limited clinical relevance, we used a cryo-tissue collection of LM from CRC patients. Patients were grouped according to their pre-operative anti-angiogenic therapy with bevacizumab (anti-VEGF) (Bev+ versus Bev– group). These groups were further divided into \pm hypertension. As only patients with hypertension are treated with RAS-inhibiting drugs, that subgroup was further subdivided into \pm RAS-inhibiting drugs. Stiffness was not affected by bevacizumab treatment alone (Figures 6A, 6B; Table S3). Within the Bev–group, anti-RAS treatment lead to a reduction in tissue stiffness when compared with non-RAS-treated hypertensive patients and to no hypertension patients (Figures 6A and 6C). Analogously, in the Bev+ group the same reductions in stiffness were observed in anti-RAS-treated patients (all $p < 0.001$) (Figures 6A and 6D). Moreover, stiffness reduction in the anti-RAS treatment group was independent of the specific treatment (Figures S6B and S6C). Bevacizumab treatment alone did not affect COL-I, α SMA, and p-MLC2, within LM (Figures 6E–6G).

(C) Immunostaining of COL-I (green) and α SMA (red) on LM cryosections.

(D) Quantification of COL-I fluorescence intensity in patients of (C) \pm HT and \pm RAS drugs ($n = 12/9/19$; $F = 12.82$, $df = 37$).^d

(E) Immunostaining of α SMA (red) and PDGFR α (green) on LM cryosections.

(F) Quantification of α SMA fluorescence intensity of (E) ($n = 12/9/19$; $F = 27.32$, $df = 37$).

(G) Immunostaining of α SMA (red) and p-MLC2 (green) on LM cryosections.

(H) Quantification of p-MLC2 fluorescence intensity of (G) ($n = 12/9/19$; $F = 39.11$, $df = 37$).

(I) Pearson correlation comparison analysis of tissue stiffness and COL-I expression, Plot showing the distribution of patients with NHT; HT + non-RAS drugs and HT + anti-RAS drugs ($n = 12/9/19$).

(J) Pearson correlation comparison analysis of ECM stiffness and α SMA expression. Plot showing patients as in (I) ($n = 12/9/19$).

(K) Pearson correlation comparison analysis of ECM stiffness and p-MLC2 expression. Plot showing patients as in (I) ($n = 12/9/19$).

In all panels: * $p < 0.05$, ** $p < 0.01$, *** $p < 0.001$. Stiffness maps, $20 \times 20 \mu\text{m}$ (A). Scale bars, $50 \mu\text{m}$ (C, E, and G). Values as mean \pm SEM and compared by one-way ANOVA multiple comparisons with Tukey's method among groups in (B), (D), (F), and (H). See also Figure S5 and Table S3.

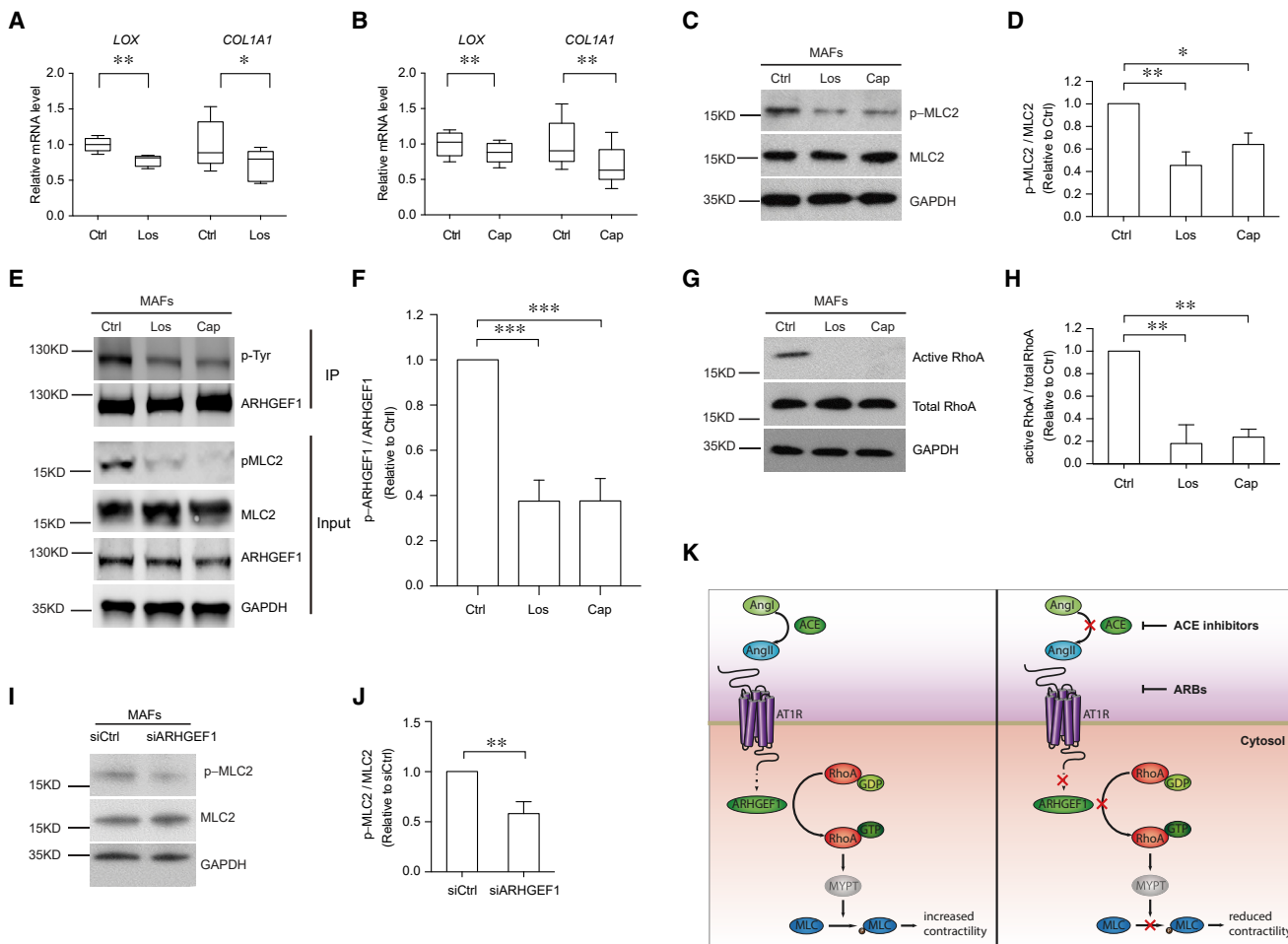


Figure 5. Anti-RAS Therapy Decreasing Matrix Deposition and Contraction of Fibroblasts

(A and B) qPCR for *LOX* and *COL1A1* after 24 h treatment with losartan (A) or captopril (B) ($n = 5$; $p = 0.0015$; $t = 7.692$, $df = 4$ and $p = 0.0418$; $t = 2.955$, $df = 4$ for losartan and $p = 0.009$; $t = 4.742$, $df = 4$ and $p = 0.002$; $t = 6.865$, $df = 4$ for captopril).

(C) Western blot of p-MLC2/MLC2 after 18 h treatment with losartan or captopril.

(D) Quantification of p-MLC2/MLC2 ratio of (C) ($n = 5$ Los/4 Cap; $p = 0.0024/0.042$; $F = 10.38$, $df = 11$).

(E) Immunoprecipitation (IP) of ARHGEF1 followed by immunoblot for p-Tyr in MAFs treated with losartan or captopril for 18 h showing reduced p-ARHGEF1.

(F) Quantification of western blot in (E) ($n = 4$ independent experiments; both $p < 0.001$; $F = 21.14$, $df = 11$).

(G) Western blot of active and total RhoA in MAFs treated with losartan or captopril for 18 h.

(H) Quantification of (G) ($n = 3$; $p = 0.003/0.005$; $F = 19.34$, $df = 6$).

(I) Western blot of p-MLC2/MLC2 in MAFs after ARHGEF1 knockdown.

(J) Quantification of (I) ($n = 5$; $p = 0.008$; $t = 3.536$, $df = 8$).

(K) Proposed working model of RAS drugs inhibiting MAF contractility.

All 10 μ M losartan or 50 μ M captopril. All panels: * $p < 0.05$, ** $p < 0.01$, *** $p < 0.001$. Values as mean \pm SEM. Values are compared by ratio paired t test in (A) and (B); unpaired Student's t test in (J) and one-way ANOVA multiple comparisons with Tukey's method among groups in (D), (F), and (H). See also Figure S6.

To assess the combined effects of anti-angiogenic therapy (bevacizumab treatment) and RAS inhibition on the vasculature, we measured vascular density in a large cohort of CRC and LM (Tables S4 and S5). The Bev+ group showed a significant $48.7\% \pm 8.2\%$ reduction in vascular density when compared with the Bev- group (Figures 6H and 6I). Similarly, the total blood vessel length was significantly reduced, and strongly correlated with vessel density (Figures S6D and S6E). Even though anti-RAS treatment alone lead to a reduction in metastases stiffness, it only slightly affected blood vessel density and length in the Bev- group (Figures 6H, 6J, and

S6F–S6H). Bevacizumab treatment reduced the vascular density in patients who were not treated with anti-RAS drugs (Figures S6I and S6J). However, vascular density (and total vascular length) in the combination treatment (anti-RAS+, Bev+) was significantly reduced by $76.6\% \pm 8.7\%$ when compared with the non-RAS, Bev+ treatment and when compared with all the Bev- groups (Figures 6H, 6K, and S6K). This was independent of the type of RAS treatment used (Figures S6L–S6N). Thus, anti-RAS drugs target tissue stiffness and thereby influence the efficacy of bevacizumab.

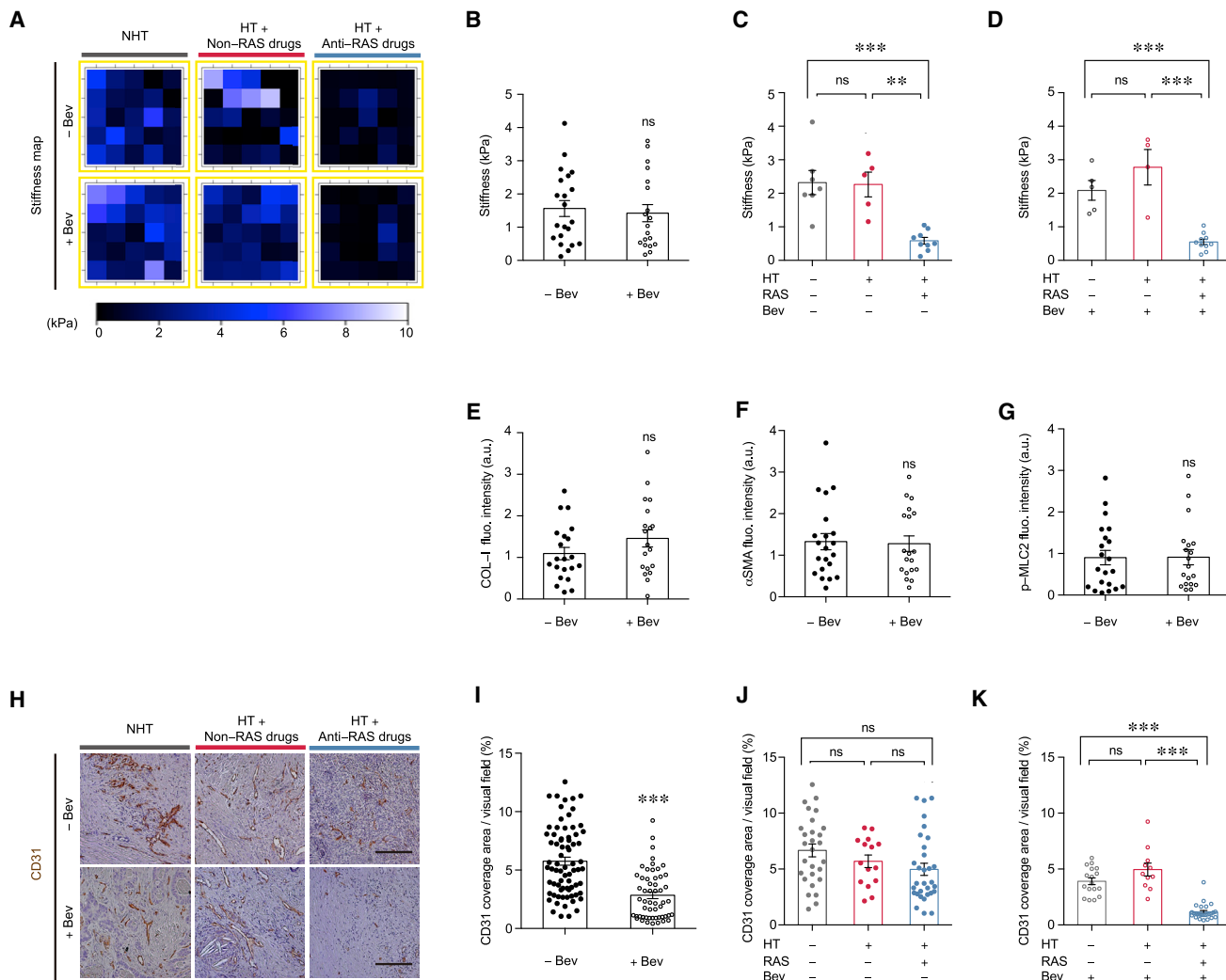


Figure 6. Anti-RAS Therapy Enhances the Effects of Bevacizumab by Reducing MAF Activation

(A) Stiffness maps of LM stroma area from mCRC patients. Bev, bevacizumab; NHT, no hypertension patients; HT, hypertension.

(B–D) Quantification of tissue stiffness: (B) \pm Bev ($n = 21$ –Bev)/ 19 +Bev; $p = 0.692$; $t = 0.3989$, $df = 38$; (C) –Bev \pm HT \pm anti-RAS drugs ($n = 7/5/9$; $F = 15$, $df = 18$); and (D) +Bev \pm HT \pm anti-RAS drugs ($n = 5/4/10$; $F = 24$, $df = 16$).

(E–G) Quantification of fluorescence intensity of (E) COL-I in patients of (Figure 4) \pm Bev ($p = 0.154$; $t = 1.456$, $df = 38$); (F) α SMA ($p = 0.854$; $t = 0.1847$, $df = 38$), and (G) p-MLC2 ($p = 0.970$; $t = 0.0378$, $df = 38$). All $n = 21$ –Bev)/ 19 +Bev.

(H) CD31 staining on LM paraffin sections.

(I–K) Quantification of percentage of CD31+ vessel area in stroma ($n = 74$ –Bev)/ 54 +Bev; $p < 0.0001$; $t = 6.386$, $df = 126$) in (I), $n = 28/15/31$; $F = 2.55$, $df = 71$ in (J), and $n = 17/11/26$; $F = 49.84$, $df = 51$ in (K).

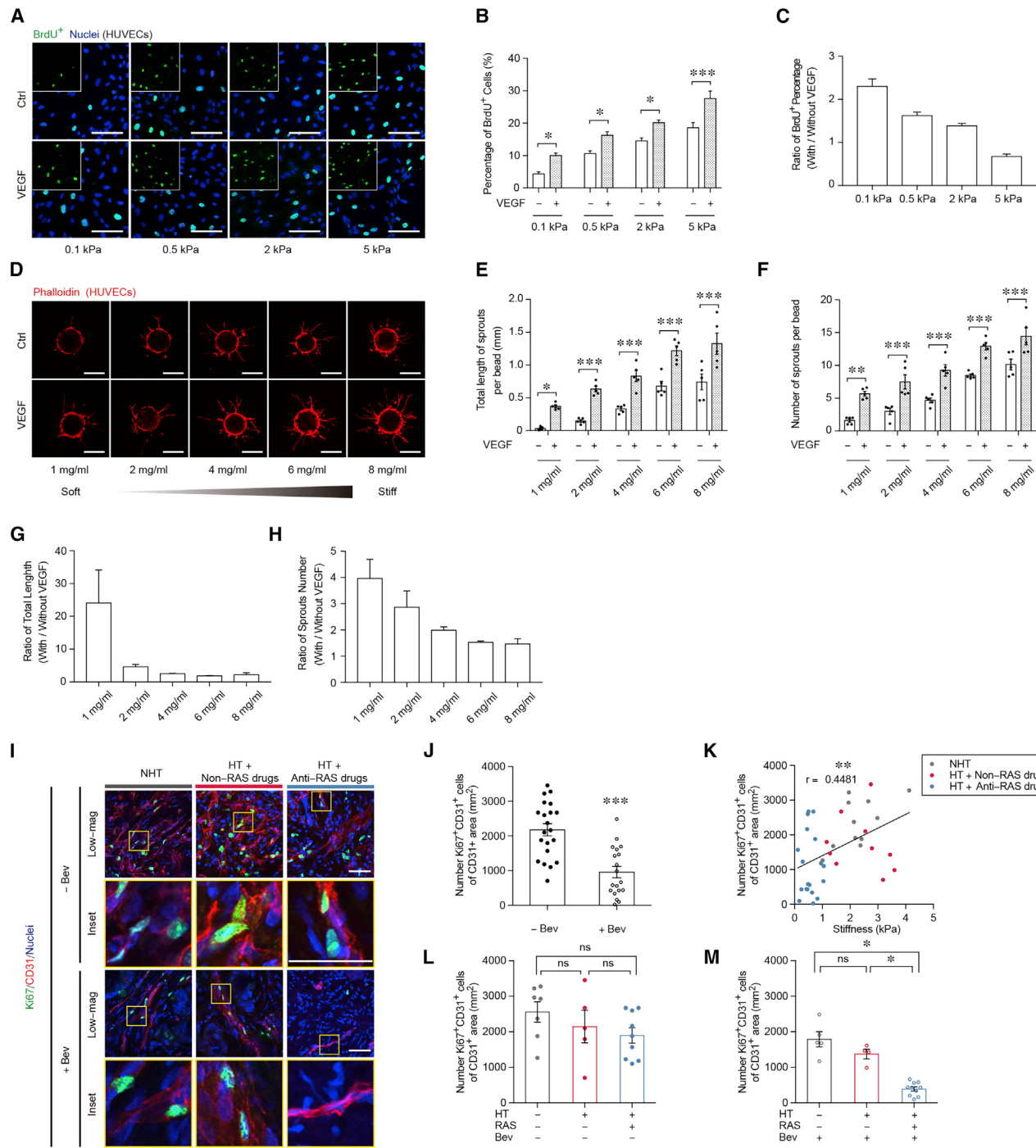
In all panels: * $p < 0.05$, ** $p < 0.01$, *** $p < 0.001$. Stiffness maps, $20 \times 20 \mu\text{m}$ (A). Scale bars $150 \mu\text{m}$ (H). Values as mean \pm SEM and compared by unpaired Student's t test in (B), (E), (F), (G), and (I) and one-way ANOVA multiple comparisons with Tukey's method among groups in (C), (D), (J), and (K); each dot represents one patient. See also Figure S6 and Tables S3–S5.

Nevertheless, the CD31+ area did not significantly correlate with pTU stiffness, which is significantly lower (Figures S6O and S6P), and was not reduced upon anti-RAS treatment (Figure S6Q).

To further understand the role of stiffness and VEGF-mediated regulation of angiogenesis, we used polyacrylamide (PA) hydrogels with different stiffness (Figure S7A). We seeded human umbilical vein endothelial cells (HUVECs) or human hepatic sinusoidal ECs (HHSECs) on hydrogel matrices with 0.1 and 0.5 kPa to mimic anti-RAS treatment and on 2 and 5 kPa to mimic stroma

without anti-RAS treatment. EC proliferation increased with stiffness, and VEGF further induced proliferation, with the highest VEGF effect at low stiffness (Figures 7A–7C and S7B–S7D).

Moreover, we analyzed EC sprouting in the presence or absence of VEGF in fibrinogen matrices of different densities (a proxy for stiffness) (Liu et al., 2018). EC sprouting (both number and length of sprouts) increased with density. VEGF led to further sprouting in all conditions with more pronounced effect of VEGF in soft matrices, as was the case for EC proliferation (Figures 7D–7H and S7E–S7I).

**Figure 7. RAS Inhibitors in Combination with Bevacizumab Inhibit EC Proliferation**

- (A) Stainings of bromodeoxyuridine (BrdU) incorporation of HUVECs on hydrogels of different stiffness ± VEGF (50 ng/mL).
- (B) Quantification of BrdU⁺ cells of (A) (n = 10 independent experiments; *p < 0.05, ***p < 0.001).
- (C) Ratio of BrdU⁺ cells in VEGF-treated/untreated groups from (B).
- (D) HUVECs sprouting assays in fibrinogen gels with different concentrations ± VEGF (50 ng/mL).
- (E and F) Quantification of total sprout length (E) and number of sprouts (F) of (D) (20 beads per condition from 5 independent experiments; *p < 0.05, **p < 0.01, ***p < 0.001).
- (G and H) Ratio of sprout length (G) and number of sprouts (H) in VEGF-treated/untreated groups.
- (I) Immunostaining of Ki67 (green) and CD31 (red) on LM cryosections.
- (J) Quantification of Ki67⁺CD31⁺ cells on LM cryosections of ± Bev-treated patients (n = 21(-Bev)/19(+Bev); p < 0.0001; t = 5.079, df = 38).
- (K) Pearson correlation comparison analysis of tissue stiffness and number of Ki67⁺CD31⁺ cells per mm² CD31⁺ area (n = 40).

(legend continued on next page)

Reduction of EC Proliferation by RAS and Angiogenesis Inhibition

To understand how the combination of anti-RAS drugs and bevacizumab affects ECs within metastases, we quantified their effect on EC proliferation. Bevacizumab treatment alone lead to a $56.1\% \pm 11.0\%$ reduction in EC proliferation (Figures 7I and 7J; Table S3). As metastases stiffness correlates with the proliferating ECs within metastases independent of the treatment (Figure 7K), we assessed if RAS inhibition was sufficient to reduce EC proliferation. In patients who did not receive anti-angiogenic treatment, RAS inhibition did not significantly reduce EC proliferation (Figure 7L); however, in patients treated with bevacizumab and anti-RAS drugs, EC proliferation was further reduced by $78.1\% \pm 9.2\%$ (Figure 7M). This reduction was independent of the type of anti-RAS drugs used (Figure S7J). Thus, while the treatment of hypertension alone does not have a significant effect on EC proliferation, anti-RAS treatment increases the efficacy of bevacizumab treatment and inhibits angiogenesis.

RAS and Angiogenesis Inhibition Improve Vessel Integrity

Tumor vessels are not only proliferating, but also structurally and functionally abnormal with a leaky EC barrier, facilitating tumor cells intravasation, and impairing chemotherapy (Jain, 2014). GSEA analysis revealed regulation of vascular permeability as a prominent feature of cluster 1 (Figure S8A). Interestingly, VEGF and matrix stiffening both potently lead to vascular permeability (Dvorak, 2002; Huynh et al., 2011). To further characterize the role of anti-RAS drugs on blood vessel integrity we analyzed their effect on EC junction stability by performing immunostaining for the tight junction protein ZO-1 (zonula occludens 1) (Mazzoni et al., 2009). While bevacizumab treatment is suggested to lead to the elimination of immature blood vessels (Jain, 2005), we observed no change in ZO-1+ tight junctions by bevacizumab (Figures 8A and 8B; Table S3). Consistent with previous findings in other disease models that increasing matrix stiffness enhance endothelial permeability (Huynh et al., 2011), we also observed a negative correlation between ZO-1+ coverage and tissue stiffness of CRC LM, suggesting a more chaotic and immature vasculature in stiffer LM (Figure 8C). In Bev+ patients treated with anti-RAS drugs, we also observed an increase in ZO-1+ coverage in ECs, suggesting that anti-RAS alone is sufficient to improve endothelial junction stability (Figures 8A and 8D). However, in the combination treatments (Bev+ and anti-RAS+) the effect on junction stability is strongly enhanced (Figures 8A and 8E), independent of the type of RAS inhibition (Figure S8B).

KLF2 is a shear stress-responsive transcriptional factor, the expression of which increases by laminar shear stress and is a sign of perfusion (Dekker et al., 2002; Wang et al., 2006). Anti-angiogenic treatment did not alter KLF2 expression in ECs (Figures 8F and 8G; Table S3). However, KLF2 expression negatively correlates with tissue rigidity, suggesting that increased stiffness impairs perfusion (Figure 8H). In patients treated without bevac-

zumab, KLF2 expression is not changed by anti-RAS treatment (Figures 8F and 8I), but is significantly higher in anti-RAS- and bevacizumab-treated patients (Figure 8F,J). Analogous anti-RAS treatment reduced hypoxia in LM of patients treated with bevacizumab (Figures S8C–S8F).

In line with those finding, in anti-RAS- and especially in anti-RAS plus bevacizumab-treated patients, erythrocytes are only visible within blood vessels and sinusoids, whereas in non-RAS-treated patients, erythrocytes are found extravascularly within the tumor tissue (Figure S8G).

In summary, the combination treatment improves blood vessel integrity, likely the result of a reduction in total EC numbers caused by bevacizumab treatment, together with a decrease in blood vessel permeability due to anti-RAS drugs.

Endothelial Cell YAP/TAZ Is a Central Hub Regulated by LM Stiffness and VEGF

YAP (Yes-associated protein) and TAZ (transcriptional coactivator with PDZ-binding motif) are crucial regulators of blood vessel growth (Kim et al., 2017; Wang et al., 2017). During development EC YAP/TAZ signaling contributes to blood vessel formation. After activation, YAP/TAZ translocate into the cell nucleus and function as a transcriptional co-factor. Because YAP/TAZ activity in ECs is regulated by VEGF and mechanical cues, such as matrix stiffness (Dupont et al., 2011; Wang et al., 2017), we tested if YAP/TAZ activation was affected by anti-RAS drugs or bevacizumab treatment. YAP/TAZ target genes (CTGF and CYR61) in isolated CD31+ ECs from LM and normal liver (Figure S8H) showed a significant upregulation in metastasis-associated endothelium, suggesting a high activation status of YAP/TAZ in LM endothelium (Figures S8I and S8J).

We aimed to understand how EC YAP/TAZ activation is affected by VEGF and matrix rigidity. *In vitro* nuclear YAP/TAZ localization in HUVECs correlates with PA hydrogel stiffness (Figures S8K and S8L). Moreover, YAP/TAZ nuclear translocation was further increased by VEGF at each tested stiffness and was reduced to stiffness baseline levels by the VEGF trap sFlt1 (Figures S8K and S8L), suggesting that lowering matrix rigidity and VEGF trapping are both required to suppress YAP/TAZ activity effectively.

We then analyzed EC YAP/TAZ activation status in patient samples using the EC nuclear marker ERG1. Anti-angiogenic treatment led to a reduction in YAP/TAZ EC nuclear intensity (Figures 8K and 8L; Table S3), suggesting that VEGF signaling was necessary for YAP/TAZ translocation in ECs in the LM. Reduction of stiffness by anti-RAS treatment did not reduce nuclear YAP/TAZ intensity by itself (Figures 8K and 8M). However, reduction of stiffness with simultaneous withdrawal of VEGF by bevacizumab treatment reduced nuclear YAP/TAZ intensity when compared with non-hypertension patients and with patients treated with bevacizumab and non-RAS drugs (Figures 8K and 8N) independent of the type of RAS inhibition (Figure S8M). In summary, anti-angiogenic therapy combined with

(L and M) Quantification of Ki67+CD31+ cells of (L) –Bev ± HT ± anti-RAS drugs patients ($n = 7/5/9$; $F = 1.406$, $df = 18$) and (M) +Bev ± HT drugs ($n = 5/4/10$; $F = 40.61$, $df = 16$) on LM cryosections.

In all panels: * $p < 0.05$, ** $p < 0.01$, *** $p < 0.001$. Scale bars, 100 μ m (A and D) and 50 μ m (I). Values as mean \pm SEM and compared by unpaired Student's t test in (J), two-way ANOVA multiple comparisons with Sidak's method among groups in (B), (E), and (F), one-way ANOVA multiple comparisons with Tukey's method among groups in (L) and (M). See also Figure S7 and Table S3.

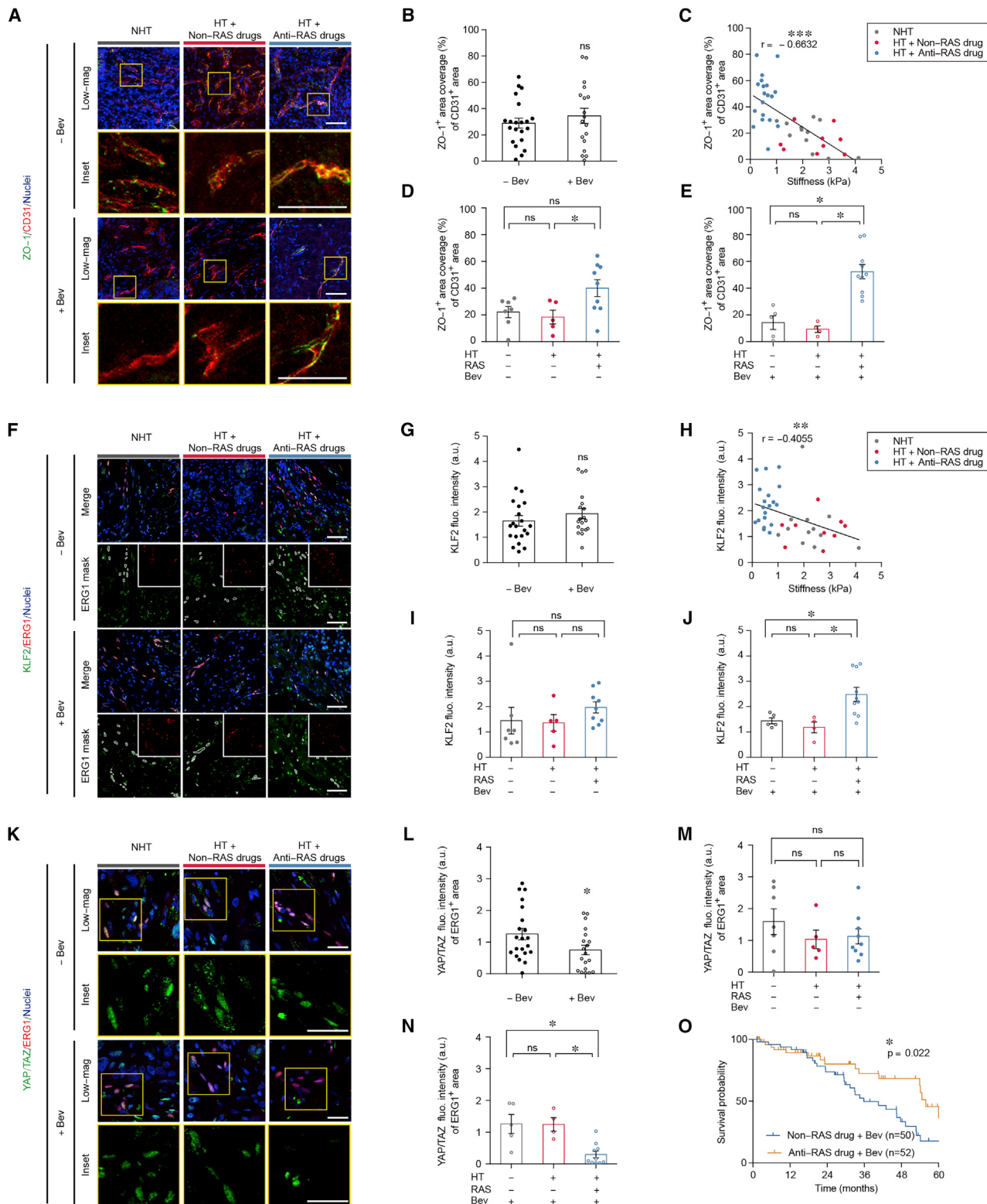


Figure 8. RAS Inhibitors in Combination with Bevacizumab Affect Vascular Integrity and Endothelial YAP/TAZ Activation

(A) Immunostaining of ZO-1 (green) and CD31 (red) on LM cryosections. Bev, bevacizumab; NHT, no hypertension patients; HT, hypertension.

(B) Quantification of ZO-1+ coverage in CD31+ areas on LM cryosections of \pm Bev-treated patients ($n = 21(-\text{Bev})/19(+\text{Bev})$; $p = 0.537$; $t = 0.6437$, df = 38).

(C) Pearson correlation comparison analysis of ZO-1+ coverage and tissue stiffness ($n = 40$).

(legend continued on next page)

RAS inhibition significantly suppresses endothelial YAP/TAZ activation and metastatic angiogenesis (Figure S8N).

RAS Inhibition with Anti-angiogenic Therapy Prolongs Survival

Most relevantly, we observed a significantly prolonged OS in patients who underwent resection of LM and received anti-angiogenic therapy with a concomitant anti-RAS treatment in the course of their disease. This was confirmed by multivariate Cox regression analysis (Figure 8O; Tables S6 and S7).

DISCUSSION

Here, we characterized the mechanical signatures of pTUs and LM from patients with CRC. Our data show that stiffness of LM in mCRC is significantly higher compared with pTU. We show that MAFs found in LM of CRC contribute significantly to tissue stiffening, through cellular contractility and ECM remodeling. Metastasis stiffness is also closely correlated with tissue vascularity, and influences the effect of anti-angiogenic therapy on intra-tumoral blood vessel reduction. Mechanical and soluble cues contribute to angiogenesis in metastases. Finally, the activity of MAFs, and therefore metastasis stiffness, can be modulated by commonly used drugs targeting the RAS, which in turn increases the efficacy of anti-angiogenic therapy. Our use of patient-derived material strengthens the clinical relevance of these findings, bypassing the need for animal model systems that only partially mimic the heterogeneous nature of tumors. This is of special importance as experimental models of colorectal LM in mice so far do not recapitulate the tissue stiffness which is observed in patients (data not shown).

Our results suggest that increased metastases stiffness plays an important role in mCRC. Myofibroblasts are key effectors in fibrogenic processes (Gascard and Tlsty, 2016; Kalluri, 2016), but targeting CAFs as a therapeutic approach needs to be considered carefully, as the consequences are not fully understood. In lung carcinoma, pancreatic adenocarcinoma, or other animal tumor models, deleting a stroma cell population expressing the fibroblast activation protein limits tumor development and progression by augmenting antitumor immunity (Kraman et al., 2010; Lo et al., 2015; Wang et al., 2014). On the contrary, depletion of a subset of α SMA+ stroma cells promotes pTU progression by inducing immunosuppression (Ozdemir et al., 2014).

These contradictory results may arise due to different microenvironments, or might be the result of the heterogeneous nature of CAFs (Li et al., 2017).

In clinical trials, matrix stiffening is inhibited by drugs targeting connective tissue growth factor (CTGF), transforming growth factor β signaling, LOX-mediated matrix crosslinking, FA kinase, nuclear factor κ B, BRAF, and MEK (Lampi and Reinhart-King, 2018). Meanwhile, RAS inhibitors, approved for treatment of hypertension and cardiovascular diseases, are used as anti-fibrotic treatments for cardiac and renal fibrosis, making our findings even more clinically relevant (Brown, 2013; Ruperez et al., 2003a, 2003b). Importantly, recent clinical trial data using neoadjuvant therapy with FOLFIRINOX and losartan showed benefits in pancreatic cancer (Murphy et al., 2019). Notably, a phase 3 trial of pamrevlumab, a monoclonal antibody that targets CTGF, was initiated recently for treating pancreatic cancer as the first “mechanotherapeutics” test in cancer therapy (Sheridan, 2019). Thus, even though we focused on mCRC, similar mechanisms could play a role in other tumor entities.

In CRC, LM MAFs express high levels of all RAS components, invoking parallels with studies showing that *in-vivo*-activated human hepatic stellate cells in cirrhotic livers express the RAS system and synthesize ANGII (Bataller et al., 2003). Circulating levels of ANGII are also increased in chronic liver disease (Bataller et al., 2000), and AT-1-mediated activation of JAK2 has been shown to induce liver fibrosis (Granzow et al., 2014). Our AFM measurements reveal that RAS inhibition reduces metastases stiffness. Similarly, patients with non-alcoholic fatty liver disease treated with RAS blockers have less-advanced hepatic fibrosis (Goh et al., 2015). We show that RAS inhibitors attenuate matrix remodeling by reducing collagen production, LOX expression, and Rho GTPase-mediated cell contractility in MAFs. In support of our data, inhibitors of LOX reduce tumor rigidity and modify tumor progression in animal models (Levental et al., 2009). As LOX is important for the premetastatic niche (Cox et al., 2015; Erler et al., 2009), RAS inhibitors may also modulate the occurrence of secondary metastases. Anti-RAS drugs also reduced tissue stiffness in pTUs, where ECM remodeling and stiffening also contribute to disease progression and prognosis (Wei et al., 2017). However, neither hypertension nor treatment with RAS inhibitors changed the stiffness of non-metastatic liver tissue (data not shown). This suggests that, before tumor cells infiltrate the liver, mechano-based therapeutics might not be beneficial. A

(D and E) Quantification of ZO-1+ coverage in CD31+ areas of (D) –Bev \pm HT \pm anti-RAS drugs ($n = 7/5/9$; $F = 4.364$, $df = 18$) and (E) +Bev \pm HT \pm anti-RAS drugs ($n = 5/4/10$; $F = 19.37$, $df = 16$) on LM cryosections.

(F) Immunostaining of KLF2 (green) and ERG1 (red) on LM cryosections.

(G) Quantification of KLF2 fluorescence intensity in ERG1+ areas on LM cryosections of \pm Bev-treated patients ($n = 21(-\text{Bev})/19(+\text{Bev})$; $p = 0.3398$; $t = 0.9667$, $df = 38$).

(H) Pearson correlation comparison analysis of KLF2 fluorescence intensity in ERG1+ areas and tissue stiffness ($n = 39$).

(I and J) Quantification of KLF2 fluorescence intensity in ERG1+ areas of (I) –Bev \pm HT \pm anti-RAS drugs ($n = 7/5/9$; $F = 0.8437$, $df = 20$) and (J) +Bev \pm HT \pm anti-RAS drugs ($n = 5/4/10$; $F = 6.797$, $df = 18$) on LM cryosections.

(K) Immunostainings of YAP/TAZ (green), ERG1 (red), and nuclei (blue) on LM cryosections.

(L–N) Quantification of YAP/TAZ fluorescence intensity in EC nucleus (ERG1) in (L) \pm Bev ($n = 21(-\text{Bev})/19(+\text{Bev})$; $p = 0.0402$; $t = 2.125$, $df = 38$); (M) –Bev \pm HT \pm anti-RAS drugs ($n = 7/5/9$; $F = 0.8482$, $df = 18$); and (N) +Bev \pm HT \pm anti-RAS drugs ($n = 5/4/10$; $F = 10.23$, $df = 16$).

(O) Kaplan-Meier curves of cumulative overall survival after surgical metastases resection of bevacizumab therapy patients receiving anti-RAS drugs or non-RAS drugs ($n = 52/50$; median survival = 55.87/35.83 months; hazard ratio [HR] = 0.52; 95% CI of ratio, 0.29–0.91).

In all panels: * $p < 0.05$, ** $p < 0.01$, *** $p < 0.001$. Scale bars, 50 μ m. Values as mean \pm SEM and compared by unpaired Student's t test in (B), (G), and (L); one-way ANOVA multiple comparisons with Tukey's method among groups in (D), (E), (I), (J), (M), and (N) and log rank (Mantel-Cox) test in (O). See also Figure S8 and Tables S3, S6, and S7.

prospective clinical trial will be useful to see whether anti-RAS could inhibit tumor progression in patients with or without metastases.

The architecture and physical microenvironment are highly abnormal in tumors, which leads to significant challenges for cancer therapy. In desmoplastic tumors, interstitial fluid pressure (IFP) is significantly increased, which pushes growth factors and cells to the peri-tumoral tissue, contributes to impaired drug delivery, and promotes tumor progression (Dewhirst and Se-comb, 2017; Heldin et al., 2004; Mitchell et al., 2017; Nia et al., 2019). Increased IFP is likely due to vessel leakiness, lymph-vessel abnormalities, interstitial fibrosis, and stroma fibroblast contraction (Heldin et al., 2004). As anti-RAS treatment reduces fibrosis and stroma fibroblast contraction, and anti-RAS plus bevacizumab increased vascular integrity in LM, patients might also benefit from reduced IFP and improved drug delivery. In addition, anti-RAS treatment can also affect other cells within the microenvironment, such as vascular smooth muscle cells, which were not the focus of this study. Of interest, both anti-RAS and anti-angiogenesis approaches were shown to enhance the effectiveness of immunotherapy (Fukumura et al., 2018; Pinter and Jain, 2017), which further highlights the potential clinical value of anti-RAS plus bevacizumab given the recent progress in immunotherapy.

It was reported that anti-VEGF treatment leads to increased expression of hyaluronic acid and glycosaminoglycans, two ECM components, which further lead to therapy resistance in mCRC (Rahbari et al., 2016). Here, an increased stiffness in mouse tumor models was seen when treated with an anti-VEGF antibody, which we did not observe in patients treated with bevacizumab. This difference may be due to differences between mouse models and human patient samples. This may also be due to the dose of anti-VEGF antibody, as the increase in stiffness was only observed with high doses of anti-VEGF antibody treatment.

We identified EC YAP/TAZ as a central hub in metastatic angiogenesis and show that, in the absence of VEGF, stiff matrices still have sufficient potency to activate YAP/TAZ in ECs, suggesting stiffness as an escape mechanism from bevacizumab treatment. We also show that reducing matrix stiffness correlates with improved blood vessel integrity, supporting previous observations that anti-RAS drugs improve blood vessel perfusion in breast cancer (Chauhan et al., 2013). These results suggest that reducing both VEGF levels and matrix stiffness are needed to reduce YAP/TAZ-mediated vessel growth and improve treatment outcomes with enhanced vessel integrity and improved perfusion.

Patients with CRC and lung cancer who develop bevacizumab-induced hypertension survive significantly longer (Nakaya et al., 2016). In our study, hypertension was recorded for all patients at the time of operation and, therefore, could include pre-existing hypertension or bevacizumab-induced hypertension. There was no survival difference between the hypertension and no hypertension population within the bevacizumab treatment group. Therefore, by itself, hypertension does not render patients more sensitive to bevacizumab. Future studies will need to evaluate if bevacizumab-induced hypertension only leads to a prolonged survival in combination with anti-RAS drugs or also other anti-hypertension drugs. Our data show that there is

a significant survival benefit in patients with hypertension who received bevacizumab and anti-RAS drugs to treat the hypertension, in accordance with previous reports (Osumi et al., 2015).

In summary, by using clinical specimens and fresh patient-derived MAFs, we have identified a new therapeutic target, MAF-mediated metastatic stiffness, for treating CRC LM. Our study also reveals that MAF-mediated matrix stiffening contributes to the development of resistance to VEGF-blocking therapy. We further show that commonly used RAS inhibitors significantly improve the efficacy of bevacizumab. Therefore, we propose that this combinatorial therapy should be considered in a neo-adjuvant setting, as well as in palliative care.

STAR METHODS

Detailed methods are provided in the online version of this paper and include the following:

- **KEY RESOURCES TABLE**
- **RESOURCE AVAILABILITY**
 - Lead Contact
 - Materials Availability
 - Data and Code Availability
- **EXPERIMENTAL MODEL AND SUBJECT DETAILS**
 - Patient Samples
 - Cell Culture
- **METHOD DETAILS**
 - Human Tissue Processing for Immunohistochemistry
 - Primary Cell Isolation
 - Immunofluorescence on Human Tissue Samples
 - Immunofluorescence of Cells in Culture
 - Atomic Force Microscopy Measurements
 - Rho Activity Assays
 - Gel Contraction Assays
 - BrdU Cell Proliferation ELISA Assay in Fibroblasts
 - BrdU Incorporation in ECs
 - Sprouting Assay
 - Polyacrylamide Gel Manufacturing
 - siRNA Transfection
 - Quantitative PCR
 - Immunoprecipitation and immunoblotting
 - RNA Sequencing and Data Analysis
 - Data Pre-Processing
 - Differential Expression and Gene Enrichment Analysis
- **QUANTIFICATION AND STATISTICAL ANALYSIS**

SUPPLEMENTAL INFORMATION

Supplemental Information can be found online at <https://doi.org/10.1016/j.ccr.2020.05.005>.

ACKNOWLEDGMENTS

This study was supported by the Deutsche Forschungsgemeinschaft (DFG) (SCHM 2560/3-1), the Ernst Jung Career Advancement Grant, and the Heidelberg Stiftung Chirurgie to T.S., by funds from the European Molecular Biology Laboratory and the DFG (DI 2205/2-1) to A.D.-M., by DFG grants from SFB1366 (project no. 394046768-SFB 1366) and from RTG-2099 to C.R.d.A., by National Natural Science Foundation of China (NSFC) grant (31871184) to X.W., and by a fellowship from the EMBL Interdisciplinary Post-doc Program (EIPOD) under Marie Curie Actions COFUND to A.I. We thank

Sascha Hinterkopf, Mareen Dupovac, and Heike Adler for technical assistance, Robert Luck for illustrations, and Victor Sarachaga for assistance with public RNA-seq data extraction. The graphic abstract was created using Servier Medical Art templates, which are licensed under a Creative Commons Attribution 3.0 Unported License; <https://smart.servier.com>. We thank the EMBL Genomics Core facility for critical assistance and advice during our RNA-seq experiments and to the EMBL advanced light microscopy facility (ALMF) for assistance with microscope imaging. We thank Dr. Qi Gao (Biomedical Computer Vision Group at Heidelberg University) for assistance with imaging analysis. Lung metastases samples were provided by Lung Biobank Heidelberg, member of the Biomaterial Bank Heidelberg (BMBH) and the biobank platform of the German Center for Lung Research (DZL).

AUTHOR CONTRIBUTIONS

Conceptualization, Y.S., X.W., A.D.-M., and T.S.; Methodology, Y.S., X.W., A.I., A.D.-M., and T.S.; Investigation, Y.S., X.W., J.L., M.S., N.M.W., N.S., A.I., A.F.V., P.R., J.L., and G.W.; Writing – Review & Editing, Y.S., X.W., C.R.A., A.D.-M., and T.S.; Funding Acquisition, C.R.A., A.D.-M., and T.S.; Resources, T.M., M.S., C.R.d.A., A.D.-M., and T.S.; Supervision, P.R., M.S., C.R.A., A.D.-M., and T.S.

DECLARATION OF INTERESTS

The authors declare no competing interests.

Received: November 26, 2018

Revised: February 12, 2020

Accepted: May 6, 2020

Published: June 8, 2020

REFERENCES

- Bai, X., Lenhart, K.C., Bird, K.E., Suen, A.A., Rojas, M., Kakoki, M., Li, F., Smithies, O., Mack, C.P., and Taylor, J.M. (2013). The smooth muscle-selective RhoGAP GRAF3 is a critical regulator of vascular tone and hypertension. *Nat. Commun.* 4, 2910.
- Bataller, R., Gines, P., Nicolas, J.M., Gorbig, M.N., Garcia-Ramallo, E., Gasull, X., Bosch, J., Arroyo, V., and Rodes, J. (2000). Angiotensin II induces contraction and proliferation of human hepatic stellate cells. *Gastroenterology* 118, 1149–1156.
- Bataller, R., Sancho-Bru, P., Gines, P., Lora, J.M., Al-Garawi, A., Sole, M., Colmenero, J., Nicolas, J.M., Jimenez, W., Weich, N., et al. (2003). Activated human hepatic stellate cells express the renin-angiotensin system and synthesize angiotensin II. *Gastroenterology* 125, 117–125.
- Bordeleau, F., Mason, B.N., Lolis, E.M., Mazzola, M., Zanotelli, M.R., Somasegar, S., Califano, J.P., Montague, C., LaValley, D.J., Huynh, J., et al. (2017). Matrix stiffening promotes a tumor vasculature phenotype. *Proc. Natl. Acad. Sci. U S A* 114, 492–497.
- Brown, N.J. (2013). Contribution of aldosterone to cardiovascular and renal inflammation and fibrosis. *Nat. Rev. Nephrol.* 9, 459–469.
- Calvo, F., Ege, N., Grande-Garcia, A., Hooper, S., Jenkins, R.P., Chaudhry, S.I., Harrington, K., Williamson, P., Moeendarbari, E., Charras, G., et al. (2013). Mechanotransduction and YAP-dependent matrix remodelling is required for the generation and maintenance of cancer-associated fibroblasts. *Nat. Cell Biol.* 15, 637–646.
- Cancer Genome Atlas, N. (2012). Comprehensive molecular characterization of human colon and rectal cancer. *Nature* 487, 330–337.
- Chauhan, V.P., Martin, J.D., Liu, H., Lacorre, D.A., Jain, S.R., Kozin, S.V., Stylianopoulos, T., Mousa, A.S., Han, X., Adstamongkonkul, P., et al. (2013). Angiotensin inhibition enhances drug delivery and potentiates chemotherapy by decompressing tumour blood vessels. *Nat. Commun.* 4, 2516.
- Chen, E.Y., Tan, C.M., Kou, Y., Duan, Q., Wang, Z., Meirelles, G.V., Clark, N.R., and Ma'ayan, A. (2013). Enrichr: interactive and collaborative HTML5 gene list enrichment analysis tool. *BMC Bioinformatics* 14, 128.
- Chien, S. (2007). Mechanotransduction and endothelial cell homeostasis: the wisdom of the cell. *Am. J. Physiol. Heart Circ. Physiol.* 292, H1209–H1224.
- Colaprico, A., Silva, T.C., Olsen, C., Garofano, L., Cava, C., Garolini, D., Sabedot, T.S., Malta, T.M., Pagnotta, S.M., Castiglioni, I., et al. (2016). TCGAbiolinks: an R/Bioconductor package for integrative analysis of TCGA data. *Nucleic Acids Res.* 44, e71.
- Colpaert, C., Vermeulen, P., Van Marck, E., and Dirix, L. (2001). The presence of a fibrotic focus is an independent predictor of early metastasis in lymph node-negative breast cancer patients. *Am. J. Surg. Pathol.* 25, 1557–1558.
- Colpaert, C.G., Vermeulen, P.B., Fox, S.B., Harris, A.L., Dirix, L.Y., and Van Marck, E.A. (2003). The presence of a fibrotic focus in invasive breast carcinoma correlates with the expression of carbonic anhydrase IX and is a marker of hypoxia and poor prognosis. *Breast Cancer Res. Treat.* 81, 137–147.
- Cox, T.R., Rumney, R.M.H., Schoof, E.M., Perryman, L., Hoye, A.M., Agrawal, A., Bird, D., Latif, N.A., Forrest, H., Evans, H.R., et al. (2015). The hypoxic cancer secretome induces pre-metastatic bone lesions through lysyl oxidase. *Nature* 522, 106–110.
- Dekker, R.J., van Soest, S., Fontijn, R.D., Salamanca, S., de Groot, P.G., Van Bavel, E., Pannekoek, H., and Horrevoets, A.J. (2002). Prolonged fluid shear stress induces a distinct set of endothelial cell genes, most specifically lung Kruppel-like factor (KLF2). *Blood* 100, 1689–1698.
- Dewhirst, M.W., and Secomb, T.W. (2017). Transport of drugs from blood vessels to tumour tissue. *Nat. Rev. Cancer* 17, 738–750.
- Dugina, V., Fontao, L., Chaponnier, C., Vasiliev, J., and Gabbiani, G. (2001). Focal adhesion features during myofibroblastic differentiation are controlled by intracellular and extracellular factors. *J. Cell Sci.* 114, 3285–3296.
- Dupont, S., Morsut, L., Aragona, M., Enzo, E., Giulitti, S., Cordenonsi, M., Zanconato, F., Le Digabel, J., Forcato, M., Bicciato, S., et al. (2011). Role of YAP/TAZ in mechanotransduction. *Nature* 474, 179–183.
- Dvorak, H.F. (2002). Vascular permeability factor/vascular endothelial growth factor: a critical cytokine in tumor angiogenesis and a potential target for diagnosis and therapy. *J. Clin. Oncol.* 20, 4368–4380.
- Erler, J.T., Bennewith, K.L., Cox, T.R., Lang, G., Bird, D., Koong, A., Le, Q.T., and Giaccia, A.J. (2009). Hypoxia-induced lysyl oxidase is a critical mediator of bone marrow cell recruitment to form the premetastatic niche. *Cancer Cell* 15, 35–44.
- Fukumura, D., Kloepper, J., Amoozgar, Z., Duda, D.G., and Jain, R.K. (2018). Enhancing cancer immunotherapy using antiangiogenics: opportunities and challenges. *Nat. Rev. Clin. Oncol.* 15, 325–340.
- Gascard, P., and Tlsty, T.D. (2016). Carcinoma-associated fibroblasts: orchestrating the composition of malignancy. *Genes Dev.* 30, 1002–1019.
- Goh, G.B., Pagadala, M.R., Dasarathy, J., Unalp-Arida, A., Sargent, R., Hawkins, C., Sourianarayanan, A., Khiyami, A., Yerian, L., Pai, R., et al. (2015). Renin-angiotensin system and fibrosis in non-alcoholic fatty liver disease. *Liver Int.* 35, 979–985.
- Grady, M.E., Composto, R.J., and Eckmann, D.M. (2016). Cell elasticity with altered cytoskeletal architectures across multiple cell types. *J. Mech. Behav. Biomed. Mater.* 61, 197–207.
- Granzow, M., Schierwagen, R., Klein, S., Kowalick, B., Huss, S., Linhart, M., Mazar, I.G., Gortzen, J., Vogt, A., Schildberg, F.A., et al. (2014). Angiotensin-II type 1 receptor-mediated Janus kinase 2 activation induces liver fibrosis. *Hepatology* 60, 334–348.
- Guilluy, C., Bregeon, J., Toumaniantz, G., Rolli-Derkinderen, M., Retailleau, K., Loufrani, L., Henrion, D., Scalbert, E., Bril, A., Torres, R.M., et al. (2010). The Rho exchange factor Arhgef1 mediates the effects of angiotensin II on vascular tone and blood pressure. *Nat. Med.* 16, 183–190.
- Guinney, J., Dienstmann, R., Wang, X., de Reynies, A., Schlicker, A., Soneson, C., Marisa, L., Roepman, P., Nyamundanda, G., Angelino, P., et al. (2015). The consensus molecular subtypes of colorectal cancer. *Nat. Med.* 21, 1350–1356.
- Hanahan, D., and Weinberg, R.A. (2011). Hallmarks of cancer: the next generation. *Cell* 144, 646–674.
- Heldin, C.H., Rubin, K., Pietras, K., and Ostman, A. (2004). High interstitial fluid pressure—an obstacle in cancer therapy. *Nat. Rev. Cancer* 4, 806–813.
- Hinz, B., Dugina, V., Ballestrem, C., Wehrle-Haller, B., and Chaponnier, C. (2003). Alpha-smooth muscle actin is crucial for focal adhesion maturation in myofibroblasts. *Mol. Biol. Cell* 14, 2508–2519.

- Hu, G., Xu, F., Zhong, K., Wang, S., Huang, L., and Chen, W. (2018). Activated tumor-infiltrating fibroblasts predict worse prognosis in breast cancer patients. *J. Cancer* 9, 3736–3742.
- Huang da, W., Sherman, B.T., and Lempicki, R.A. (2009). Systematic and integrative analysis of large gene lists using DAVID bioinformatics resources. *Nat. Protoc.* 4, 44–57.
- Humphrey, J.D., Dufresne, E.R., and Schwartz, M.A. (2014). Mechanotransduction and extracellular matrix homeostasis. *Nat. Rev. Mol. Cell Biol.* 15, 802–812.
- Huynh, J., Nishimura, N., Rana, K., Peloquin, J.M., Califano, J.P., Montague, C.R., King, M.R., Schaffer, C.B., and Reinhart-King, C.A. (2011). Age-related intimal stiffening enhances endothelial permeability and leukocyte transmigration. *Sci. Transl Med.* 3, 112ra122.
- Ingber, D.E. (2002). Mechanical signaling and the cellular response to extracellular matrix in angiogenesis and cardiovascular physiology. *Circ. Res.* 91, 877–887.
- Jain, R.K. (2005). Normalization of tumor vasculature: an emerging concept in antiangiogenic therapy. *Science* 307, 58–62.
- Jain, R.K. (2014). Antiangiogenesis strategies revisited: from starving tumors to alleviating hypoxia. *Cancer Cell* 26, 605–622.
- Jayson, G.C., Kerbel, R., Ellis, L.M., and Harris, A.L. (2016). Antiangiogenic therapy in oncology: current status and future directions. *Lancet* 388, 518–529.
- Ji, X., Bosse, Y., Landi, M.T., Gui, J., Xiao, X., Qian, D., Joubert, P., Lamontagne, M., Li, Y., Gorlov, I., et al. (2018). Identification of susceptibility pathways for the role of chromosome 15q25.1 in modifying lung cancer risk. *Nat. Commun.* 9, 3221.
- Jonsson, K., Grondahl, G., Salo, M., Tingstedt, B., and Andersson, R. (2012). Repeated liver resection for colorectal liver metastases: a comparison with primary liver resections concerning perioperative and long-term outcome. *Gastroenterol. Res. Pract.* 2012, 568214.
- Kagan, H.M., and Li, W. (2003). Lysyl oxidase: properties, specificity, and biological roles inside and outside of the cell. *J. Cell Biochem.* 88, 660–672.
- Kai, F., Laklai, H., and Weaver, V.M. (2016). Force matters: biomechanical regulation of cell invasion and migration in disease. *Trends Cell Biol.* 26, 486–497.
- Kalluri, R. (2016). The biology and function of fibroblasts in cancer. *Nat. Rev. Cancer* 16, 582–598.
- Kamangar, F., Dores, G.M., and Anderson, W.F. (2006). Patterns of cancer incidence, mortality, and prevalence across five continents: defining priorities to reduce cancer disparities in different geographic regions of the world. *J. Clin. Oncol.* 24, 2137–2150.
- Kim, J., Kim, Y.H., Kim, J., Park, D.Y., Bae, H., Lee, D.H., Kim, K.H., Hong, S.P., Jang, S.P., Kubota, Y., et al. (2017). YAP/TAZ regulates sprouting angiogenesis and vascular barrier maturation. *J. Clin. Invest.* 127, 3441–3461.
- Klughammer, J., Kiesel, B., Roetzer, T., Fortelny, N., Nemc, A., Nenning, K.H., Furtner, J., Sheffield, N.C., Datlinger, P., Peter, N., et al. (2018). The DNA methylation landscape of glioblastoma disease progression shows extensive heterogeneity in time and space. *Nat. Med.* 24, 1611–1624.
- Kraman, M., Bambrough, P.J., Arnold, J.N., Roberts, E.W., Magiera, L., Jones, J.O., Gopinathan, A., Tuveson, D.A., and Fearon, D.T. (2010). Suppression of antitumor immunity by stromal cells expressing fibroblast activation protein-alpha. *Science* 330, 827–830.
- Kuchnio, A., Moens, S., Brunning, U., Kuchnio, K., Cruys, B., Thienpont, B., Broux, M., Ungureanu, A.A., Leite de Oliveira, R., Bruyere, F., et al. (2015). The cancer cell oxygen sensor PHD2 promotes metastasis via activation of cancer-associated fibroblasts. *Cell Rep.* 12, 992–1005.
- Kuleshov, M.V., Jones, M.R., Rouillard, A.D., Fernandez, N.F., Duan, Q., Wang, Z., Koplev, S., Jenkins, S.L., Jagodnik, K.M., Lachmann, A., et al. (2016). Enrichr: a comprehensive gene set enrichment analysis web server 2016 update. *Nucleic Acids Res.* 44, W90–W97.
- Kuo, J.C., Han, X., Hsiao, C.T., Yates, J.R., 3rd, and Waterman, C.M. (2011). Analysis of the myosin-II-responsive focal adhesion proteome reveals a role for beta-Pix in negative regulation of focal adhesion maturation. *Nat. Cell Biol.* 13, 383–393.
- Lacolley, P., Regnault, V., Segers, P., and Laurent, S. (2017). Vascular smooth muscle cells and arterial stiffening: relevance in development, aging, and disease. *Physiol. Rev.* 97, 1555–1617.
- Laklai, H., Miroshnikova, Y.A., Pickup, M.W., Collisson, E.A., Kim, G.E., Barrett, A.S., Hill, R.C., Lakins, J.N., Schlaepfer, D.D., Mouw, J.K., et al. (2016). Genotype tunes pancreatic ductal adenocarcinoma tissue tension to induce multicellular fibrosis and tumor progression. *Nat. Med.* 22, 497–505.
- Langmead, B., and Salzberg, S.L. (2012). Fast gapped-read alignment with Bowtie 2. *Nat. Methods* 9, 357–359.
- Lampi, M.C., and Reinhart-King, C.A. (2018). Targeting extracellular matrix stiffness to attenuate disease: from molecular mechanisms to clinical trials. *Sci. Transl Med.* 10, <https://doi.org/10.1126/scitranslmed.aoa0475>.
- Levental, K.R., Yu, H., Kass, L., Lakins, J.N., Egeblad, M., Erler, J.T., Fong, S.F., Csiszar, K., Giaccia, A., Weninger, W., et al. (2009). Matrix crosslinking forces tumor progression by enhancing integrin signaling. *Cell* 139, 891–906.
- Li, H., Courtois, E.T., Sengupta, D., Tan, Y., Chen, K.H., Goh, J.J.L., Kong, S.L., Chua, C., Hon, L.K., Tan, W.S., et al. (2017). Reference component analysis of single-cell transcriptomes elucidates cellular heterogeneity in human colorectal tumors. *Nat. Genet.* 49, 708–718.
- Liberzon, A., Birger, C., Thorvaldsdottir, H., Ghandi, M., Mesirov, J.P., and Tamayo, P. (2015). The Molecular Signatures Database (MSigDB) hallmark gene set collection. *Cell Syst.* 1, 417–425.
- Liu, Y., Lv, J., Liang, X., Yin, X., Zhang, L., Chen, D., Jin, X., Fiskesund, R., Tang, K., Ma, J., et al. (2018). Fibrin stiffness mediates dormancy of tumor-repopulating cells via a Cdc42-driven Tet2 epigenetic program. *Cancer Res.* 78, 3926–3937.
- Lo, A., Wang, L.S., Scholler, J., Monslow, J., Avery, D., Newick, K., O'Brien, S., Evans, R.A., Bajor, D.J., Clenderin, C., et al. (2015). Tumor-promoting desmoplasia is disrupted by depleting FAP-expressing stromal cells. *Cancer Res.* 75, 2800–2810.
- Lopez, J.I., Kang, I., You, W.K., McDonald, D.M., and Weaver, V.M. (2011). In situ force mapping of mammary gland transformation. *Integr. Biol. (Camb)* 3, 910–921.
- Love, M.I., Huber, W., and Anders, S. (2014). Moderated estimation of fold change and dispersion for RNA-seq data with DESeq2. *Genome Biol.* 15, 550.
- Mammoto, A., Connor, K.M., Mammoto, T., Yung, C.W., Huh, D., Aderman, C.M., Mostoslavsky, G., Smith, L.E., and Ingber, D.E. (2009). A mechanosen-sitive transcriptional mechanism that controls angiogenesis. *Nature* 457, 1103–1108.
- Mazzone, M., Dettori, D., Leite de Oliveira, R., Loges, S., Schmidt, T., Jonckx, B., Tian, Y.M., Lanahan, A.A., Pollard, P., Ruiz de Almodovar, C., et al. (2009). Heterozygous deficiency of PHD2 restores tumor oxygenation and inhibits metastasis via endothelial normalization. *Cell* 136, 839–851.
- Mitchell, M.J., Jain, R.K., and Langer, R. (2017). Engineering and physical sciences in oncology: challenges and opportunities. *Nat. Rev. Cancer* 17, 659–675.
- Mohammadi, H., and Sahai, E. (2018). Mechanisms and impact of altered tumour mechanics. *Nat. Cell Biol.* 20, 766–774.
- Mouw, J.K., Ou, G., and Weaver, V.M. (2014). Extracellular matrix assembly: a multiscale deconstruction. *Nat. Rev. Mol. Cell Biol.* 15, 771–785.
- Murphy, J.E., Wo, J.Y., Ryan, D.P., Clark, J.W., Jiang, W., Yeap, B.Y., Drapek, L.C., Ly, L., Baglini, C.V., Blaszkowsky, L.S., et al. (2019). Total neoadjuvant therapy with FOLFIRINOX in combination with losartan followed by chemoradiotherapy for locally advanced pancreatic cancer: a phase 2 clinical trial. *JAMA Oncol.* 5, 1020–1027.
- Nakaya, A., Kurata, T., Yokoi, T., Iwamoto, S., Torii, Y., Katahira, Y., Ogata, M., Hamada, M., Kon, M., and Nomura, S. (2016). Retrospective analysis of bevacizumab-induced hypertension and clinical outcome in patients with colorectal cancer and lung cancer. *Cancer Med.* 5, 1381–1387.
- Nia, H.T., Munn, L.L., and Jain, R.K. (2019). Mapping physical tumor microenvironment and drug delivery. *Clin. Cancer Res.* 25, 2024–2026.
- Northcott, J.M., Dean, I.S., Mouw, J.K., and Weaver, V.M. (2018). Feeling stress: the mechanics of cancer progression and aggression. *Front. Cell Dev. Biol.* 6, 17.

- Northey, J.J., Przybyla, L., and Weaver, V.M. (2017). Tissue force programs cell fate and tumor aggression. *Cancer Discov.* 7, 1224–1237.
- Oakes, P.W., Beckham, Y., Stricker, J., and Gardel, M.L. (2012). Tension is required but not sufficient for focal adhesion maturation without a stress fiber template. *J. Cell Biol.* 196, 363–374.
- Osterreicher, C.H., Penz-Osterreicher, M., Grivennikov, S.I., Guma, M., Koltsova, E.K., Datz, C., Sasik, R., Hardiman, G., Karin, M., and Brenner, D.A. (2011). Fibroblast-specific protein 1 identifies an inflammatory subpopulation of macrophages in the liver. *Proc. Natl. Acad. Sci. U.S.A.* 108, 308–313.
- Osumi, H., Matsusaka, S., Wakatsuki, T., Suenaga, M., Shinozaki, E., and Mizunuma, N. (2015). Angiotensin II type-1 receptor blockers enhance the effects of bevacizumab-based chemotherapy in metastatic colorectal cancer patients. *Mol. Clin. Oncol.* 3, 1295–1300.
- Ozdemir, B.C., Pentcheva-Hoang, T., Carstens, J.L., Zheng, X., Wu, C.C., Simpson, T.R., Laklai, H., Sugimoto, H., Kahlert, C., Novitskiy, S.V., et al. (2014). Depletion of carcinoma-associated fibroblasts and fibrosis induces immunosuppression and accelerates pancreas cancer with reduced survival. *Cancer Cell* 25, 719–734.
- Parkin, D.M. (2001). Global cancer statistics in the year 2000. *Lancet Oncol.* 2, 533–543.
- Paszek, M.J., Zahir, N., Johnson, K.R., Lakins, J.N., Rozenberg, G.I., Gefen, A., Reinhart-King, C.A., Margulies, S.S., Dembo, M., Boettiger, D., et al. (2005). Tensional homeostasis and the malignant phenotype. *Cancer Cell* 8, 241–254.
- Pausch, T.M., Aue, E., Wirsik, N.M., Freire Valls, A., Shen, Y., Radhakrishnan, P., Hackert, T., Schneider, M., and Schmidt, T. (2020). Metastasis-associated fibroblasts promote angiogenesis in metastasized pancreatic cancer via the CXCL8 and the CCL2 axes. *Sci. Rep.* 10, 5420.
- Pickup, M.W., Mouw, J.K., and Weaver, V.M. (2014). The extracellular matrix modulates the hallmarks of cancer. *EMBO Rep.* 15, 1243–1253.
- Pinato, D.J., Ramachandran, R., Toussi, S.T., Vergine, M., Ngo, N., Sharma, R., Lloyd, T., Meeran, K., Palazzo, F., Martin, N., et al. (2013). Immunohistochemical markers of the hypoxic response can identify malignancy in phaeochromocytomas and paragangliomas and optimize the detection of tumours with VHL germline mutations. *Br. J. Cancer* 108, 429–437.
- Pinter, M., and Jain, R.K. (2017). Targeting the renin-angiotensin system to improve cancer treatment: implications for immunotherapy. *Sci. Transl. Med.* 9, <https://doi.org/10.1126/scitranslmed.aan5616>.
- Pletscher-Frankild, S., Palleja, A., Tsafou, K., Binder, J.X., and Jensen, L.J. (2015). DISEASES: text mining and data integration of disease-gene associations. *Methods* 74, 83–89.
- Rahbari, N.N., Kedrin, D., Incio, J., Liu, H., Ho, W.W., Nia, H.T., Edrich, C.M., Jung, K., Daubriac, J., Chen, I., et al. (2016). Anti-VEGF therapy induces ECM remodeling and mechanical barriers to therapy in colorectal cancer liver metastases. *Sci. Transl. Med.* 8, 360ra135.
- Rahbari, N.N., Reissfelder, C., Schulze-Bergkamen, H., Jager, D., Buchler, M.W., Weitz, J., and Koch, M. (2014). Adjuvant therapy after resection of colorectal liver metastases: the predictive value of the MSKCC clinical risk score in the era of modern chemotherapy. *BMC Cancer* 14, 174.
- Reed, N.I., Jo, H., Chen, C., Tsujino, K., Arnold, T.D., DeGrado, W.F., and Sheppard, D. (2015). The alphavbeta1 integrin plays a critical in vivo role in tissue fibrosis. *Sci. Transl. Med.* 7, 288ra279.
- Ruperez, M., Lorenzo, O., Blanco-Colio, L.M., Esteban, V., Egido, J., and Ruiz-Ortega, M. (2003a). Connective tissue growth factor is a mediator of angiotensin II-induced fibrosis. *Circulation* 108, 1499–1505.
- Ruperez, M., Ruiz-Ortega, M., Esteban, V., Lorenzo, O., Mezzano, S., Plaza, J.J., and Egido, J. (2003b). Angiotensin II increases connective tissue growth factor in the kidney. *Am. J. Pathol.* 163, 1937–1947.
- Schaefer, C.F., Anthony, K., Krupa, S., Buchoff, J., Day, M., Hannay, T., and Buetow, K.H. (2009). PID: the pathway interaction database. *Nucleic Acids Res.* 37, D674–D679.
- Sheridan, C. (2019). Pancreatic cancer provides testbed for first mechanotherapeutics. *Nat. Biotechnol.* 37, 829–831.
- Subramanian, A., Tamayo, P., Mootha, V.K., Mukherjee, S., Ebert, B.L., Gillette, M.A., Paulovich, A., Pomeroy, S.L., Golub, T.R., Lander, E.S., et al. (2005). Gene set enrichment analysis: a knowledge-based approach for interpreting genome-wide expression profiles. *Proc. Natl. Acad. Sci. U.S.A.* 102, 15545–15550.
- Taylor, I. (1996). Liver metastases from colorectal cancer: lessons from past and present clinical studies. *Br. J. Surg.* 83, 456–460.
- Tommelein, J., Verset, L., Boterberg, T., Demetter, P., Bracke, M., and De Wever, O. (2015). Cancer-associated fibroblasts connect metastasis-promoting communication in colorectal cancer. *Front. Oncol.* 5, 63.
- Vaziri, N.D., and Rodriguez-Iturbe, B. (2006). Mechanisms of disease: oxidative stress and inflammation in the pathogenesis of hypertension. *Nat. Clin. Pract. Nephrol.* 2, 582–593.
- Wang, L.C., Lo, A., Scholler, J., Sun, J., Majumdar, R.S., Kapoor, V., Antzis, M., Cotner, C.E., Johnson, L.A., Durham, A.C., et al. (2014). Targeting fibroblast activation protein in tumor stroma with chimeric antigen receptor T cells can inhibit tumor growth and augment host immunity without severe toxicity. *Cancer Immunol. Res.* 2, 154–166.
- Wang, N., Miao, H., Li, Y.S., Zhang, P., Haga, J.H., Hu, Y., Young, A., Yuan, S., Nguyen, P., Wu, C.C., et al. (2006). Shear stress regulation of Kruppel-like factor 2 expression is flow pattern-specific. *Biochem. Biophys. Res. Commun.* 341, 1244–1251.
- Wang, X., Freire Valls, A., Schermann, G., Shen, Y., Moya, I.M., Castro, L., Urban, S., Solecki, G.M., Winkler, F., Riedemann, L., et al. (2017). YAP/TAZ orchestrate VEGF signaling during developmental angiogenesis. *Dev. Cell* 42, 462–478.e7.
- Wei, B., Zhou, X., Liang, C., Zheng, X., Lei, P., Fang, J., Han, X., Wang, L., Qi, C., and Wei, H. (2017). Human colorectal cancer progression correlates with LOX-induced ECM stiffening. *Int. J. Biol. Sci.* 13, 1450–1457.
- Weitz, J., Koch, M., Debus, J., Hohler, T., Galle, P.R., and Buchler, M.W. (2005). Colorectal cancer. *Lancet* 365, 153–165.
- Yeh, Y.T., Hur, S.S., Chang, J., Wang, K.C., Chiu, J.J., Li, Y.S., and Chien, S. (2012). Matrix stiffness regulates endothelial cell proliferation through septin 9. *PLoS One* 7, e46889.
- Yoshihara, K., Shahmoradgoli, M., Martinez, E., Vegesna, R., Kim, H., Torres-Garcia, W., Trevino, V., Shen, H., Laird, P.W., Levine, D.A., et al. (2013). Inferring tumour purity and stromal and immune cell admixture from expression data. *Nat. Commun.* 4, 2612.

STAR★METHODS

KEY RESOURCES TABLE

REAGENT or RESOURCE	SOURCE	IDENTIFIER
Antibodies		
Collagen-I	Abcam	Cat#ab34710; RRID: AB_731684
α SMA	Sigma-Aldrich	Cat#C6198; RRID: AB_476856
PDGFR α	Cell signaling	Cat#3174; RRID: AB_2162345
p-MLC2	Cell signaling	Cat#3671; RRID: AB_330248
CD31	Abcam	Cat#ab9498; RRID: AB_307284
YAP/TAZ	Cell signaling	Cat#8418; RRID: AB_10950494
ERG1	Abcam	Cat#ab214341
ZO-1	invitrogen	Cat#61-7300; RRID: AB_138452
KLF2	Abcam	Cat#Ab203591
Vinculin	Abcam	Cat#ab129002; RRID: AB_11144129
Ki67	Abcam	Cat#GTX16667; RRID: AB_422351
MLC2	Cell signaling	Cat#3672; RRID: AB_10692513
ARHGEF1	Cell signaling	Cat#3669; RRID: AB_2059739
GAPDH	Santa Cruz	Cat#sc-47724; RRID: AB_627678
HIF-1 α	Novus	Cat#NB100-479; RRID: AB_10000633
anti-phosphotyrosine (4G10) antibody	Millipore	Cat#05-321; RRID: AB_309678
anti-BrdU antibody	Oxford Biotechnology	Cat#OBT0030; RRID: AB_609568
anti-fibroblasts Microbeads	Miltenyi Biotec	Cat#130-050-601
CD45+ Microbeads	Miltenyi Biotec	Cat#130-045-801
CD31+ Microbeads	Miltenyi Biotec	Cat#130-091-935
Alexa Fluor 488-conjugated donkey anti-rabbit	Jackson ImmunoResearch	Cat#711-545-152; RRID: AB_2313584
Alexa Fluor 488-conjugated goat anti-rabbit	invitrogen	Cat#A11008; RRID: AB_143165
Alexa Fluor 568-conjugated goat anti-mouse	invitrogen	Cat#A11031; RRID: AB_144696
Alexa Fluor 488-conjugated goat anti-rat	Molecular Probes	Cat#A21208; RRID: AB_141709
Alexa Fluor 647-conjugated donkey anti-mouse	Jackson ImmunoResearch	Cat#715-605-151; RRID: AB_2340863
HRP donkey anti-rabbit antibody	Jackson ImmunoResearch	Cat#711-035-152; RRID: AB_10015282
HRP donkey anti-mouse antibody	Jackson ImmunoResearch	Cat#715-035-150; RRID: AB_2340770
HRP donkey anti-goat antibody	Jackson ImmunoResearch	Cat#705-035-147; RRID: AB_2313587
Bacterial and Virus Strains		
eGFP adenovirus	Vectorlab	Cat#1060
Chemicals, Peptides, and Recombinant Proteins		
VEGF	Prof.Peter Carmeliet	N/A
COL-I	Corning™	Cat#354249
Matrigel	Corning™	Cat#354230
fibrinogen	Sigma	Cat#F-8630
Losartan	Cayman	Cat#10006594
Captopril	Cayman	Cat#15313
PD123319	Cayman	Cat#136676-91-0
CGP-42112	MedChemExpress	Cat#HY-12405
Fibronectin	Sigma Aldrich	Cat#F0895
Sulfo-SANPAH	Pierce	Cat#22589

(Continued on next page)

Continued

REAGENT or RESOURCE	SOURCE	IDENTIFIER
DAPI	Invitrogen	Cat#D1306
ToPRO-3 iodide	invitrogen	Cat#T3605
Phalloidin	Sigma Aldrich	Cat#P1951
Critical Commercial Assays		
ELISA BrdU Kit	Roche	Cat#11-647-229-001
RhoA Pull-down Activation Assay	Cytoskeleton	Cat#BK036
Biochem Kit		
Deposited Data		
Gene expression profile	This paper	GEO: GSE145432
TCGA data	TCGA	https://portal.gdc.cancer.gov/
Experimental Models: Cell Lines		
HUVECs	Promocells	Cat#C-12200
HHSECs	ScienCell	Cat#CRL3216
Oligonucleotides		
Human ARHGEF1 siRNA:	Dharmacon	Cat#L-009421-00-0005
Primers, see Table S8	This paper	N/A
Software and Algorithms		
NIH ImageJ	NIH	N/A
R	N/A	https://www.r-project.org
Bowtie2 software	Langmead and Salzberg, 2012	http://bowtie-bio.sourceforge.net/bowtie2/index.shtml
CellHesion 200	JPK	N/A
Prism 7.0 software	GraphPad	N/A
GSEA	Broad Institute	http://software.broadinstitute.org/gsea/index.jsp
Enrichr	Ma'ayan Laboratory	https://amp.pharm.mssm.edu/Enrichr/
Ggsurvplot (ggplot2)	Alboukadel Kassambara	https://www.rdocumentation.org/packages/survminer/versions/0.4.6
DAVID	Huang da et al., 2009	https://david.ncifcrf.gov/
GraphPad Prism 7.0a Software	GraphPad Software	N/A
ESTIMATE Algorithmus	Yoshihara et al., 2013	N/A
Pathway activities Estimate Algorithmus	Guinney et al., 2015	N/A
PID Algorithmus	Schaefer et al., 2009	N/A
DISEASE Algorithmus	Pletscher-Frankild et al., 2015	N/A
Molecular Signatures Database (MSigDB)	Broad Institute	http://software.broadinstitute.org/gsea/msigdb

RESOURCE AVAILABILITY

Lead Contact

Further information and requests for resources and reagents should be directed to and will be fulfilled by the Lead Contact Thomas Schmidt (thomas.schmidt1@med.uni-heidelberg.de).

Materials Availability

This study did not generate new unique reagents.

Data and Code Availability

The accession number for the RNA-seq data reported in this paper is GEO: GSE145432. RNA-Seq gene expression data and patient clinical data from 451 patients with colon adenocarcinoma (TCGA-COAD) were downloaded with the R package “TCGAbiolinks” ([Colaprico et al., 2016](#)) from the GDC Data Portal (<https://portal.gdc.cancer.gov/>).

EXPERIMENTAL MODEL AND SUBJECT DETAILS

Patient Samples

Samples from patients with CRC liver metastases (LM), lung metastases (LungM) and patients with primary colorectal cancer (pTU) were analyzed. All patients underwent planned curative surgery at the department for General, Visceral and Transplantation Surgery and department of Thoracic Surgery at the University Hospital Heidelberg. The study was approved by the local ethics committee (S-080/2013 and 323/2004). Informed consent was obtained from all patients. Tissue samples of 128 LM, 9 LungM and 36 pTU patients were used for immunohistochemistry ([Tables S3](#) and [S4](#)). 40 fresh from the operating room snap-frozen human LM-CRC, 9 LungM and 36 pTU-CRC tissues were collected from patients who underwent surgery between 2007 and 2019 ([Table S3](#)). Of 12 patients with pTU (n=6) and LM (n=6) CAFs and MAFs were isolated for RNA-Seq analysis ([Table S1](#)), 22 patients with pTU (n=12 and LM (n=10) tumor tissue were used for RNA-Seq analysis ([Table S1](#)). Survival and multivariate analysis were performed from a set of 102 patients treated with bevacizumab ([Tables S5](#) and [S6](#)). Patient data and samples were collected in a prospective database and analyzed retrospectively. All patient data was pseudonymized.

Cell Culture

Human umbilical vein endothelial cells (HUVECs) were purchased from (PromoCell, Germany; C-12200). Human hepatic sinusoid endothelial cells (HHSECs) were purchased from (ScienCell, Carlsbad, CA). HUVECs and HHSECs were maintained in 0.1% porcine gelatin (Sigma-Aldrich, Germany; G9136) coated flasks and cultured in Endopan 3 Kit (PAN-Biotech, Germany; P04-0010K) supplemented with 10% FBS (Gibco®, USA; 10500), 100 U/mL penicillin and 100 mg/mL streptomycin (both Gibco®, USA; 15140122). To obtain conditioned medium from all cell types, cells were starved for 48 h in 2% FBS growth factor-free Endopan medium (PAN-Biotech, Germany; P04-0010K). For culturing CAFs and MAFs after isolation, cells were maintained in 20%FBS DMEM (Sigma-Aldrich, Germany; D5796). HUVECs from passages 3 to 5 were used for the experiments. HHSECs from passages 1 to 2 were used for the experiments. For studying the signaling pathways involved and for gel contraction and sprouting assays CAFs and MAFs from passages 2 to 5 were used.

METHOD DETAILS

Human Tissue Processing for Immunohistochemistry

Tumor and non-tumor tissue samples were collected freshly from the operation theater, fixed in 4% PFA, placed in ethanol and embedded in paraffin. Tissue samples were sliced in 5 µm thick sections, deparaffinized with xylene, rehydrated with ethanol and incubated with Target Retrieval Solution (Dako, Denmark; S1699). 0.3% hydrogen peroxide in methanol was used to inhibit endogenous peroxidase. The blocking step was performed with 2% BSA (SERVA, Germany; 11930) and 0.3% Triton-X100 (Sigma-Aldrich, Germany; T8787) in PBS. Primary antibodies were incubated over night at 4°C: αSMA (1:400; Sigma-Aldrich, Germany; A2547), CD31 (1:100; Abcam, UK; ab9498) HIF-1α (1:200 ; Novus; NB100-479). After washing, the appropriate biotinylated secondary antibodies were incubated for 45 min: HRP donkey anti-rabbit antibody (1:200; Jackson ImmunoResearch, USA; 711-035-152), HRP donkey anti-mouse antibody (1:200; Jackson ImmunoResearch, USA; 715-035-150). Amplification was done with a TSA biotin detection kit (Perkin-Elmer, USA; NEL700001KT) and signal detection with a liquid DAB+ substrate chromogenic system (Dako, Denmark; K3468). Counterstaining was done with hematoxylin and mounted with Eukitt quick-hardening mounting medium (Sigma-Aldrich, Germany; 03989). Stainings were performed on consecutive sections. Images were obtained with an AxioStar Plus microscope (Zeiss, Germany). 5 pictures of randomly chosen visual field were taken from each section with an 20X magnification using an AxioCam MRc (Zeiss, Germany). Images were analyzed with NIH ImageJ 1.51s. Positive areas were measured in CD31 and αSMA stainings. The quantification of HIF-1α was performed as previously described ([Pinato et al., 2013](#)), the intensity of staining was scored as 1(low), 2(medium) and 3(high), H-score was assigned using the formula: [1 × (% cells 1+) + 2 × (% cells 2+) + 3 × (% cells 3+)], the final score ranging from 0-300 indicates the expression of HIF-1α in each patient.

Primary Cell Isolation

Primary cells were isolated by using a Magnetic cell separation method (Miltenyi Biotec, Germany) according to the manufacturer's instructions. Briefly, freshly collected tissue from the operation theater, was transported in Hank's Balanced Salt Solution (HBSS, Gibco®, USA; 14025134), cut into small pieces and incubated with Collagenase I (200 U/ml; Worthington Biochem, USA; LS004197), DNase I (150 U/ml; Roche, Germany; 10104159001) and Hyaluronidase (200 U/ml; Sigma-Aldrich, Germany; H3506) in HBSS for 30 min at 37°C with 700 rpm. The solution was forced through a 100 µm cell strainer followed by a 70 µm cell strainer washed several times with PEB buffer (0.5% BSA and 2 mM EDTA in PBS). For isolating fibroblasts, the single cell suspension was incubated with anti-fibroblast MicroBeads in PEB buffer for 15 min at 4°C and then applied on two separation columns (LS/MS, Miltenyi Biotec, Germany; 130-042-401/130-042-201) in a magnetic field (MidiMACS™, Germany; 130-042-301). The non-fibroblast fraction was washed out of the columns with PEB buffer. For culturing, fibroblasts were maintained in DMEM media containing 20% FCS. All experiments were performed up to five passages to avoid possible gross genomic changes during long-term *in vitro* culture. Cells were verified by fibroblastic or myofibroblastic morphology in two dimensions (2D), expression of stromal marker Vimentin, activated marker αSMA and ability to contract gels (3D). For isolation of endothelial cells, the single cell suspension was fibroblast and immune cell depleted with anti-fibroblasts Microbeads (Miltenyi Biotec, Germany; 130-050-601) followed by an immune

cell depletion by CD45⁺ beads (Miltenyi Biotec, Germany; 130-045-801). Next, we enriched for endothelial cells by CD31⁺ beads (Miltenyi Biotec, Germany; 130-091-935).

Immunofluorescence on Human Tissue Samples

For pre-fixed tissues, the samples were fixed in 4% PFA over-night, then dehydrated inside 30% sucrose (Sigma-Aldrich, Germany; S0389) in PBS and then placed and embedded in O.C.T. medium (Leica, Germany; 0201-08926) before freezing in liquid nitrogen. For post fixed tissues, the fresh tissue surface was dehydrated before liquid nitrogen snap freezing. 10 µm thick sections were fixed in 4% PFA for 15 min on slides. For all immunostainings, tissue sections were washed with PBS and then blocked in 2% BSA and 0.3% Triton X-100 in PBS for 60 min at room temperature (RT). Sections were then incubated with primary antibodies overnight at 4°C: αSMA (1:400, Sigma-Aldrich, Germany; C6198), PDGFRα (1:100 Cell signaling, USA; 3174), p-MLC2 (1:100, Cell signaling, USA; 3671), COL-I (1:100, Abcam, UK; ab34710), YAP/TAZ (1:200, Cell signaling, USA; 8418) or ERG1 (1:200, Abcam, UK; ab214341), CD31 (1:100, Abcam, UK; ab9498), ZO-1 (1:100, Invitrogen, USA; 61-7300), KLF2 (1:100, Abcam, UK; ab203591), Fibronogen (1:100, Abcam, UK; ab118533), followed by incubation with fluorochrome-conjugated secondary antibodies for 90 min at RT: Alexa Fluor 488-conjugated donkey anti-rabbit (1:400; Jackson ImmunoResearch, USA; 711-545-152), Alexa Fluor 488-conjugated goat anti-rabbit (1:400; Invitrogen, USA; A11008), Alexa Fluor 568-conjugated goat anti-mouse (1:400; Invitrogen, USA; A11031), Alexa Fluor 647-conjugated donkey anti-mouse (1:400; Jackson ImmunoResearch, USA; 715-605-151). 2% BSA and 0.3% Triton X-100 in PBS was used to dilute primary and secondary antibodies. DAPI (1:1000; Invitrogen, USA; P1306) and To-Pro-3 (1:1000; Invitrogen, USA; T3605) were used to stain cell nuclei. Trichrome staining was performed by using a commercial kit (HT15-1KT). All stainings were quantified using NIH ImageJ 1.51s analysis software with the same threshold for each stain; positivity was analyzed in five visual fields for each sample. Negative controls were performed for each sample without adding any primary antibodies. Pictures were taken with a LSM 510 META laser-scanning microscope (Zeiss, Germany).

Immunofluorescence of Cells in Culture

CAFs or MAFs were seeded on coverslips. HUVECs and HHSECs were seeded on PA gels. After desired treatment, cells were fixed with 4% PFA in PBS for 15 min at RT. Afterwards, cells were permeabilized with 0.2% Triton X-100 in PBS, blocked in 2% BSA and 0.2% Triton X-100 in PBS, and incubated with primary antibodies: YAP/TAZ, (1:400; Cell signaling, USA; 8418), αSMA (1:400; Sigma-Aldrich, Germany; C6198), PDGFRα (1:200; Cell signaling, USA; 3174), p-MLC2 (1:200; Cell signaling, USA; 3671), Vinculin, (1:400; Abcam, UK; ab129002). After washing, cells were incubated with Alexa-Fluro secondary antibodies. Images were acquired using a confocal microscope (Zeiss, Germany; LSM 510). More than 4 fields of view from at least three independent experiments were randomly chosen. For analyzing YAP/TAZ subcellular localization, cells presenting preferential nuclear YAP/TAZ localization, equal nuclear or cytoplasmic, or mainly cytoplasmic YAP/TAZ localization were counted blindly.

Atomic Force Microscopy Measurements

Atomic force microscopy (AFM) and analysis were performed as previously described (Laklai et al., 2016; Lopez et al., 2011). AFM settings and tissue sample preparation were optimized using freshly resected liver metastases and cryo-preserved tissues. Snap frozen tissue blocks were cut into 30 µm thick sections. Prior to AFM measurements, each section was immersed in PBS and thawed at RT. Samples were maintained in proteinase inhibitor (cOmplete, Roche, Germany; 11873580001) in PBS supplemented with DAPI during the AFM session. 36 samples from primary colorectal cancer (pTU), 40 samples from liver metastases of colorectal cancer (LM) and 9 samples from lung metastases of colorectal cancer (LungM) were used to measure the Young's elastic modulus of the cancer-associated stroma (Table S3). Considering the heterogeneity of the tumors, in the three cases (pTU, Liver metastases and Lung metastases), tissue stiffness was always measured in the vascularized tumor stroma to reduced intra-tumoral variability. AFM indentations were performed using a CellHesion 200 from JPK mounted on a Nikon Ti inverted fluorescent microscope. Briefly, we used silicon nitride cantilevers with a spring constant of 0.03 N/m (Bruker, USA; MLCT) and attached a borosilicate glass spherical ball of 10 µm in diameter (Novascan Tech, USA; PT.GS) using epoxy glue (Araldite, Switzerland). Cantilevers were calibrated using the thermal oscillation method before each experiment. Samples were approached at 4 µm/s and intended at a 0.4 µm/s rate, with a maximum force of 2 nN. Cantilevers were tapping on the matrix of the tumor stroma. Five 20 µm x 20 µm AFM force maps were typically obtained on each sample, each map as a 5 x 5 raster series of indentations using the JPK software. The Hertz model was used to determine the elastic properties of the tissue. The upper 200 nm of tissue were considered for all fits. Tissue samples were assumed to be incompressible and a Poisson's ratio of 0.5 was used in the calculation of the Young's elastic modulus.

Rho Activity Assays

RhoA activity assays were performed by using a RhoA Pull-down Activation Assay Biochem Kit (Cytoskeleton, USA; BK036) according to the manufacturer's instructions. Briefly, CAFs or MAFs were treated with losartan, captopril or vehicle for 18 h. Cells were washed with ice-cold PBS, lysed in provided lysis buffer, centrifuged and snap frozen in liquid nitrogen. After examining the total protein concentration of lysates, cell lysates were incubated with Rhokin-RBD beads (25 µg on a rotator for 1 h at 4 degrees), washed with provided Washing Buffer and boiled with 2 x Laemmli sample buffer for 2 min. The samples were analyzed by western blot. Data was processed as a ratio of active RhoA/total RhoA; the values of the control group were set to 1.

Gel Contraction Assays

To quantify active gel contraction, MAFs and CAFs (2.5×10^4 cells) were embedded in 100 μl of collagen type I (CorningTM, USA; 354249)/Matrigel (CorningTM, USA; 354230), yielding a final collagen concentration of 4 mg/ml and a final Matrigel concentration of 2 mg/ml in 96-well plates. Once the gel polymerized (1 h), cells were washed once in 10% FBS DMEM for 1 h and then replaced with fresh media containing the different treatments. Gel contraction was monitored over 48 h by taking photographs under a stereomicroscope (Leica M12). To obtain the gel contraction value, the relative diameters of the well and the gel were measured using ImageJ software, and the percentage of contraction was calculated using the formula $100 \times (\text{well area} - \text{gel area})/\text{well area}$.

BrdU Cell Proliferation ELISA Assay in Fibroblasts

The colorimetric immunoassay for quantification of cell proliferation was performed by using an ELISA BrdU Kit (Roche, Germany; 11-647-229-001) according to the manufacturer's instructions as previously done (Pausch et al., 2020). Briefly, 5×10^3 CAFs or MAFs per well were plated in a 96 well plate. Cells were allowed to attach overnight, and stimulated with losartan, captopril or vehicle for 24 h. Cells were then washed with PBS and incubated with fixation/denaturation solution for 30 min. After that, the fixation/denaturation solution was removed and the culture was incubated with anti-BrdU working solution (1:1000 dilution) for 90 min. After washing, 100 μl of the color reaction substrate solution was added for 30 min. Last 25 μl of 1 M H₂SO₄ was added for 1 min on a shaking platform to stop the reaction. Measurements of absorption at 450 nm were immediately performed using a fluorimeter (Infinite 200 Pro; TECAN, Switzerland; 30050303).

BrdU Incorporation in ECs

To analyze EC proliferation *in vitro*, HUVECs or HHSECs were plated on PA hydrogels. After overnight starvation, cells were treated with or without VEGF (50 ng/ml) for 24 h. BrdU (10 μM) was added and incubation of the cultures continued for 4 h at 37°C. Cells were fixed in 4% PFA/PBS for 20 min and permeabilized and blocked in 2% BSA 0.3% Triton X-100/PBS for 30 min at RT. After unmasking with ice-cold HCl, neutralization with Na₂HPO₄ buffer for 10 min was done prior to primary antibody incubation. An anti-BrdU antibody (1:250, OBT0030, Oxford Biotechnology) was incubated in blocking solution overnight at 4°C and an appropriate Alexa FluorTM-conjugated secondary antibody was incubated for 2 h at RT. Nuclei were counterstained with DAPI (1:1000, D1306, Invitrogen). Cells were mounted and imaged in a confocal microscope (Zeiss LSM780). All experiments were quantified blind to experimental conditions.

Sprouting Assay

COL-I gel sprouting assays were performed as previously described (Kuchnio et al., 2015; Paszek et al., 2005). In brief, HUVECs were infected with eGFP adenovirus (100 MOI; Vectorlab, Pennsylvania, USA). After 24 h, GFP-labelling of all cells was confirmed by imaging with a fluorescence microscope. Cytodex 3 microcarrier beads (GE Healthcare, Sweden; 17-0485-01) were incubated with GFP expressing HUVECs (mixed at 200 cells per bead). In conditioned medium (CM) and co-culture (CC) on top groups: The coated beads were then embedded in a COL-I (2 mg/ml; CorningTM, USA; 354249) and Matrigel (1 mg/ml; CorningTM, USA; 354230) gels in a 48-well plate. In CC inside groups: The coated beads were mixed fibroblasts (ratio of fibroblasts/endothelial cells=4:1) and embedded in the same gel mixture. Gels were polymerized in a 37°C incubator for 30 min, followed by addition of 0.5 ml of conditioned medium or starvation medium (ENDOPAN3 with 2% FBS). Fibrin gel bead sprouting assay was performed as previously described (Wang et al., 2017). HUVECs or HHSECs were coated with cytodec 3 microcarrier beads and embedded in gradient concentration of fibrin gels (fibrinogen, Calbiochem), 0.625 Units/mL thrombin (Sigma-Aldrich) and 0.15 Units/mL aprotinin (Sigma-Aldrich). After 24 h the culture was fixed with 4% PFA for 15 min, blocked in 1% BSA, 0.2% TritonX-100-PBS and stained with 1 $\mu\text{g}/\text{mL}$ Phalloidin-fluo (Sigma-Aldrich, Germany; P1951) for 2 h. Confocal images were taken with a Zeiss LSM 510 microscope. Sprout length and number of sprouts were analyzed by NIH ImageJ 1.51s. 20 beads per condition were analyzed for each independent experiment.

Polyacrylamide Gel Manufacturing

Polyacrylamide gels were prepared as previously described (Yeh et al., 2012). Briefly, solutions were prepared by using acrylamide (40% w/v solution; Sigma-Aldrich, Germany; A4058) and bis-acrylamide crosslinker (2% w/v solution, Sigma-Aldrich, Germany; 111-26-9). Gels with different stiffness were prepared by varying the final concentrations of acrylamide and bis-acrylamide. The mixtures containing acrylamide and bis-acrylamide were degassed for 15 min to remove oxygen from the solutions. To polymerize the mixtures, 30 μl of 10% w/v ammonium persulfate (Bio-Rad, USA; 1610700) and 20 μl of N,N,N,N'-tetramethylethylenediamine (TEMED; Bio-Rad, USA; 1610800) were added to yield a final volume of 5 ml. A 50–70 μm -thick gel was casted. The results on substrate stiffness were determined by atomic force microscopy (Figure S7A). To allow cell adhesion, gel surfaces were activated by exposing the heterobifunctional crosslinker Sulfo-SANPAH (Pierce, USA; 22589) at 0.5 mg/mL in 50 nM HEPES (Sigma-Aldrich, Germany; H3375) to UV light. After activation, the gels were washed with PBS to remove excess crosslinker. Gels were then coated with 0.015 mg/mL fibronectin (Sigma-Aldrich, Germany; F0895) at 37°C for 1 h or overnight at 4°C.

siRNA Transfection

MAFs were seeded in a 6 well plate. After 16 h 30-50% confluence cells were transfected with control siRNA (MISSION® siRNA Universal Negative Control by Sigma-Aldrich, Germany; SIC001) or siRNA for ARHGEF1 (ON-TARGET plus smart pool; Dharmacon, UK; L-009421-00-0005) using Oligofectamine (Invitrogen, USA; 12252011) according to the manufacturer's instructions. The final concentration of siRNA solution was 200 nM. After 48 h cells were harvested for analysis.

Quantitative PCR

Cells were harvested for RNA extraction using Trizol (Invitrogen, USA; 15596018) or the mini RNA extraction kit (Qiagen, Germany; 74106). RNA samples were reverse-transcribed to complementary DNA (cDNA) using Maxima Reverse Transcriptase (Thermo Fisher Scientific, USA; EP0741) or SuperScript VILO cDNA Synthesis Kit (Invitrogen, USA; 11-754-050). qPCR was performed using Fast SYBR Green Master Mix (Roche, USA; 04887352001) and the 7300 real-time PCR system (Applied Biosystems). GAPDH or 18S rRNA were used as internal controls. All qPCR results were obtained from at least 3 biological replicates. Primers used for qPCR were produced by Invitrogen and are listed in [Table S8](#).

Immunoprecipitation and immunoblotting

For detection of p-ARHGEF1, Co-IP assays were performed as previously described ([Wang et al., 2017](#)). Cells were lysed using mild lysis buffer (20 mM Tris at pH 7.5, 150 mM NaCl, 5 mM EDTA, 1% NP-40, 10% Glycerol, 1X protease inhibitor cocktail and 1X phosphatase inhibitor (Roche)). Cell lysates were centrifuged for 10 min, and supernatants were used for immunoprecipitation. ARHGEF1 was immunoprecipitated using anti-ARHGEF1 antibody (Cell Signaling). An anti-phosphotyrosine (4G10) antibody (Millipore) was used to detect p-Tyr of ARHGEF1 by immunoblotting.

RNA Sequencing and Data Analysis

To compare the transcriptome difference of LM and pTU, 12 pTU and 10 LM tissue were used for generating RNAseq data. To compare the transcriptome difference of MAFs and CAFs, 6 MAFs and 6 CAFs isolates from 12 different patients at passage 1 were used for generating RNAseq data. Total RNA was isolated by using mini RNA isolation kit (Qiagen, Germany; 74106). Sequencing was performed by the GeneCore at the EMBL (Heidelberg, Germany) on an Illumina HiSeq 2000 platform using the Truseq stranded mRNA kit from Illumina. Quality was assessed on an Agilent 2100 Bioanalyzer. RNA-Seq libraries were prepared according to the manufacturer's protocol (Illumina TruSeq RNA sample preparation v2).

Data Pre-Processing

Raw mRNA sequencing reads (fastq format) of LM vs. pTU and MAFs vs. CAFs were mapped on the galaxy server with the Salmon Transcript Quantification package (version 0.9.1) to the Homo sapiens genome assembly GRCh38 (hg38). The heatmap was drawn as described above. Ward.D2 was used as the clustering method. Correlation and Canberra distances were measured for clustering the columns and rows, respectively.

Differential Expression and Gene Enrichment Analysis

Raw RNA-seq count tables were imported to DEseq2 for differential expression analysis ([Love et al., 2014](#)). LM was compared with TU as shown in [Figure 2A](#). MAFs were compared with CAFs as shown in [Figure 2E](#). Cluster 1 was compared with cluster 7 as shown in [Figure S2B](#). The corresponding survival curve was drawn with ggsurvplot in R ([Klughammer et al., 2018](#)). The top 1000 significantly up-regulated genes from each comparison group were used for enrichment analysis. Enrichment analysis based on GO term and KEGG was performed by DAVID (version 6.8) (<https://david.ncifcrf.gov/>) ([Huang da et al., 2009](#)). Enrichment analysis based on PID ([Schaefer et al., 2009](#)) and DISEASE([Pletscher-Frankild et al., 2015](#)) was performed by Enrichr ([Kuleshov et al., 2016](#)), using an R interface (<https://github.com/definitelysean/enrichR>, as those two databases were not included inside DAVID database. Enrichment results with adjusted p values (Benjamini-Hochberg procedure) less than 0.1 (FDR <10%) were shown. GSEA plots were done using the GSEA program (version 3.0). The following signature collections were used: "hallmark", "KEGG" and "GO" from the Molecular Signatures Database (MSigDB) ([Liberzon et al., 2015](#)) (<http://software.broadinstitute.org/gsea/msigdb>). We only used gene sets whose number of genes was more than 21 ([Ji et al., 2018](#)). The combined score was calculated using the formula combine score = z-score x $-\log_{10}$ (p value).

Pathway activities for each cluster, as shown in [Figure S2D](#), were estimated with a method developed by Justin Guinney ([Guinney et al., 2015](#)). Gene sets of interest were identified by the consortium and separated in five main groups (as detailed in [Table S2](#)): among those groups, ESTIMATE represents gene expression signatures for inferring the fraction of stromal and immune cells in tumor samples ([Yoshihara et al., 2013](#)).

QUANTIFICATION AND STATISTICAL ANALYSIS

All experiment statistical analyses were performed using GraphPad Prism 7.0a software (GraphPad Software). The R statistical framework, version 3.5.1 (<https://www.r-project.org>) was used for sequencing data analysis. Results are presented as the mean \pm s.e.m. of biological replicates. Each dot represents a biological replicate. Statistical methods for comparison of experimental group in each experiment are indicated in the figure legends. All clinical analyses were performed using SPSS (USA; version 24). Survival

analysis was performed using the Log-rank (Mantel-Cox) test. P value <0.05 are considered significant. * $p < 0.05$, ** $p < 0.01$, *** $p < 0.001$. For the descriptive analysis on cohorts (OS analysis, paraffin fixed tissue, snap frozen tissue, primary isolated fibroblasts sequencing), demographic and clinicopathological characteristics (gender, age, UICC stage, primary tumor local invasion (pT), regional lymph node spreading (pN), MSKCC score, recurrence time < 12 months, biomarker expression (CEA) before hepatectomy, pattern of metastases, size of metastases, primary tumor site and chemotherapy and adjuvant chemotherapy) were evaluated with descriptive statistics. Univariate survival analysis was performed using the Kaplan-Meier method, with survival differences calculated with the log-rank test. To determine whether anti-RAS drugs are an independent predictive factor for response to bevacizumab-based chemotherapy, the Cox regression model was used and adjusted for recurrence time, pattern of metastases and MSKCC score.